

2-METER SPARK CHAMBER MAGNET MODEL FOR THE DETERMINATION
OF FIELD DISTRIBUTION IN SPACE

by

H. Brechna, E. Burfine, R. Mizrahi, A. Wolff

January 1966

Technical Report
Prepared Under
Contract AT(04-3)-515
for the USAEC
San Francisco Operations Office

Printed in USA. Price \$ 3.00. Available from the Clearinghouse for Federal
Scientific and Technical Information (CFSTI), National Bureau of Standards,
U. S. Department of Commerce, Springfield, Virginia.

TABLE OF CONTENTS

	<u>Page</u>
I. Introduction	1
II. Conceptual Design	2
A. Coils	2
B. Iron Shell	7
C. Forces	16
III. The Electromagnetic Model	20
A. Symmetric Magnet	23
B. Model with Lower Pole Only	23
C. Model with One Pole and Modified Upper Yoke	34
D. Model with One Pole and Modified Upper Yoke Representing Final 2-Meter Spark Chamber Magnet	34
IV. Comparison Between Measurement and Calculations	42
V. Model Measurements	50
A. System Operation	50
B. Field Measurements	55
 Appendix A Axial and Radial Fields of Coaxial Solenoid Pairs . . .	 56
Appendix B The Geometrical Model	60
Appendix C The Electromagnetic Model	62
References	64

LIST OF FIGURES

	<u>Page</u>
1. 2-m spark chamber magnet	6
2. Geometry factors versus α and β for constant current distribution . .	8
3. Magnetic dipole configuration	10
4. Calculated axial distribution of the axial magnetic field	13
5. Calculated radial distribution of the axial magnetic field	14
6. Radial distribution of the radial field	15
7. 1/10 scale spark chamber magnet model	21
8. Magnetization curves of M-6 cold reduced silicon iron and low carbon ingot iron	22
9. 1/10 scale spark chamber symmetric magnet model with 14 double pancakes	24
10. Magnetization curves of different model magnet configurations	25
1. BI curve for symmetric magnet shown in Figure 9.	
2. BI curve for magnet illustrated in Figure 16.	
3. BI curve for magnet according to Figure 19.	
4. BI curve for magnet according to Figure 23 and true replica of the 2-m spark chamber magnet.	
5. BI curve for magnet according to Figure 23, but distance between upper and lower horizontal yoke unchanged from Figure 19.	
11. B_z distribution along the X axis for variations excitation levels for the symmetric model magnet	26
12. B_z distribution along the Y axis for the symmetric model magnet . . .	27
13. Saturation curve of the vertical yoke (symmetric model Fig. 9)	28
14. B_z distribution in different planes parallel to the pole surface (symmetric model Fig. 9)	29
15. Inductance versus current (symmetric model Fig. 9)	30
16. Asymmetric 1/10 scale model magnet. Upper pole removed. Coils adjusted to compensate for the iron asymmetric configuration. Number of double pancakes 14	31
17. B_z along the Y axis for different excitation levels (magnet according to Fig. 15)	32
18. Inductance versus excitation current (magnet according to Fig. 15) . .	33
19. Asymmetric model magnet. Upper pole removed. The upper yoke is provided with an opening of 8". Coils adjusted. Number of double pancakes 14	35
20. B_z distribution along X axis (magnet model Fig. 19)	36

LIST OF FIGURES - Cont.

	<u>Page</u>
21. B_z distribution along Y axis (magnet model Fig. 19)	37
22. Magnet inductance versus current (magnet model Fig. 19)	38
23. Asymmetric model magnet (true 1/10 scale spark chamber magnet model shown in Fig. 1). Upper pole removed. Upper yoke provided with an opening of 8" diameter. Number of double pancakes is reduced from 14 to 10 length of vertical yokes reduced to keep the gap height constant to 4".	39
24. B_z versus Z axis for various magnet currents	40
25. B_r versus X, Y measured in the median plane (magnet according to Fig. 2)	41
26. B_z along X axis (model magnet Fig. 23)	43
27. B_z along Y axis (model magnet Fig. 23)	44
28. B_z versus X axis measured at Z = 0.635 cm above the pole surface . .	45
29. B_z versus X measured at Z = 10.8 cm above the pole surface	46
30. B_z versus Z axis above the upper yoke	47
31. Magnet inductance versus excitation current (model magnet Fig. 23) .	48
32. Magnet pulser circuit	51
33. Magnet control system	52
34. Circuit to measure the radial field component	53
35. Axial field and current oscillograms	54
36. Radial field and peak current oscillograms	54
37. Coil representation for calculation purposes	57

LIST OF SYMBOLS

a	Coil radius
a_1	Coil inner radius
a_2	Coil outer radius
A	Magnetic vector potential
b_1, b_2	Half axial coil length
B	Magnetic flux density
C	Capacitance
F	Fabry factor for split coils
G	Coil Fabry factor (also called geometry factor)
h	Mech dimension
H	Magnetic intensity
I	Current
ℓ	Axial length
L	Inductance
N	Number of turns
P	Power
r	Radial dimension
S	Current density
t	Time
x, y, z	Coordinates
Z	Impedance
α	Ratio $\frac{a_2}{a_1}$
β_1	Ratio $\frac{b_1}{a_1}$
β_2	Ratio $\frac{b_2}{a_1}$
$a_1 \gamma_1, a_1 \gamma_2$	Axial space from gap center to individual coil center, $a_1 \gamma_1 = \delta + b_1$; $a_1 \gamma_2 = \delta + b_2$
δ	Half axial gap width between coil sections
λ	Space factor
μ	Permeability
ν	Mesh number
ρ	Resistivity
Φ	Flux
ϕ, θ, ψ	angle

ABSTRACT

A 1/10-scale electromagnetic model of the 2-meter spark chamber magnet to be used at the End Station A area at SLAC was built to determine the axial and radial magnetic field distribution inside and outside the gap. Starting with a symmetric iron core and uniform distribution of ampere-turns on both poles, the model was changed gradually to the form which complies with the present design of the 2-meter spark chamber magnet. The report describes field measurements performed on all models starting with the symmetric case.

I. INTRODUCTION

Experimentation on scale models of convenient size is wide-spread in the fields of mechanical and electrical engineering. In magnet engineering little model work has been done on scale models and the references on the subject are few.¹

Due to the complexity of the 2-meter spark chamber magnet and the limitations of our present computer program, assuming either the two-dimensional or the axial symmetric case (SLAC-Nutcracker Program),² it was decided to build a 1/10-scale geometrical or electromagnetic model, which could easily be changed to different configurations and adapted to the different uses of the actual magnet.

From two candidate magnet types, dc and ac magnets, the ac magnet with its laminated core was chosen. The magnet was energized from a 60-kilojoule capacitor bank.

In geometrical models, all pertinent dimensions of the original are scaled down by the same scale-length factor, in order to obtain the corresponding dimensions in the model. In iron magnets the actual permeability must also be scaled.

This approach has a few disadvantages, as outlined below:

a. The time scale must be equal to the length scale (Appendix B). Thus, for our 1/10-scale model, the wavelength should be 10 times faster than the original. This means that an ac magnet with an arbitrarily chosen pulse shape can not be used.

b. The simulation of the iron core and its nonlinear (H-B) characteristics is not possible.

c. To match fields, the resistivity scale in the conductor should be equal to the length scale. This means that the coil resistivity of our model had to be 10 times smaller, which requires LN₂-cooled OFHC copper conductors.

For our model, we used the electromagnetic model³ with arbitrary pulse time scale, but scaled geometrical dimensions of the core and coil.

The electromagnetic model consists of two parts:

- a. An equivalent circuit of capacitances, of scale factor C.
 - b. A geometrical model for the self and mutual inductances of scale factor L.
- For nonlinear inductances, the iron core is scaled geometrically.

With an appropriate voltage scale, the same magnetic characteristic B in the gap and permeability μ are present at corresponding points of the magnet and model. The relationship between the various scale factors of the electromagnetic model is described in Appendix C; however, the respective characteristics of the magnet and model are given in Table I.

Table II shows calculated and measured (Appendix C) values for the dimensionless parameters.

II. CONCEPTUAL DESIGN

A. Coils

In an earlier report⁵ R. Mozley described the magnet configuration and basic requirements. The magnet is being designed to provide a large volume of magnetic field, readily accessible for viewing and placing spark chambers, and ease in assembly. The provision that the magnet may be used with either two poles or a single pole is also included in the design requirements. The double pancakes can be exchanged between upper and lower pole in order to provide as much axial field homogeneity as possible.

The optimal coil shape is calculated as shown in Appendix A.

The field and power ratio for an adapted split coil configuration with set parameters for a_1 and δ is calculated from Eq. (1):

$$B(0,0,0) = \frac{\sqrt{2\pi}}{10} \cdot \frac{1}{\left[(\alpha^2 - 1)(\beta_1 + \beta_2)\right]^{\frac{1}{2}}} \cdot \left\{ -\frac{2\delta}{a_1} \cdot \ln \frac{\alpha + \left[\alpha^2 + \left(\frac{\delta}{a_1}\right)^2\right]^{\frac{1}{2}}}{1 + \left[1 + \left(\frac{\delta}{a_1}\right)^2\right]^{\frac{1}{2}}} \right. \\ \left. + \left(2\beta_1 + \frac{\delta}{a_1}\right) \cdot \ln \frac{\alpha + \left[\alpha^2 + \left(2\beta_1 + \frac{\delta}{a_1}\right)^2\right]^{\frac{1}{2}}}{1 + \left[1 + \left(2\beta_1 + \frac{\delta}{a_1}\right)^2\right]^{\frac{1}{2}}} \right. \\ \left. + \left(2\beta_2 + \frac{\delta}{a_1}\right) \cdot \ln \frac{\alpha + \left[\alpha^2 + \left(2\beta_2 + \frac{\delta}{a_1}\right)^2\right]^{\frac{1}{2}}}{1 + \left[1 + \left(2\beta_2 + \frac{\delta}{a_1}\right)^2\right]^{\frac{1}{2}}} \right\} \cdot \sqrt{\frac{P \cdot \lambda}{a_1^3}} \quad (1)$$

TABLE I
2-METER SPARK CHAMBER AND MODEL CHARACTERISTICS

	<u>2-Meter Magnet</u>	<u>20-cm Model</u>
Central field strength (kG)	15	15
Pole diameter (meters)	2	0.20
Gap height (meters)	1	0.1
Coil i. d. (meters)	2.23	0.2254
Coil o. d. (meters)	3.6	0.361
Turns per double pancake	33	30
Number of double pancakes		
Upper pole	7	7
Lower pole	3	3
Conductor dimensions (cm)	4.57×3.81	0.4114×0.4114
Conductor cross section (cm ²)	13.19	0.16
Magnet current peak (amperes)	11,050	1210
Voltage at peak current (volts)	511.5	450.1
Pulse duration (seconds)	-	70×10^{-3}
Magnet resistance (ohms)	4.63×10^{-2}	0.3 ^(a)
Magnet inductance (Henry)	0.3 (calc)	23×10^{-3}
Magnet capacitance (F)	15×10^{-6}	520×10^{-12}
Iron weight (kg)	266.36×10^3	421
Coil weight (kg)	36.36×10^3	40

(a) The equivalent magnet ac resistance is calculated from $\frac{R_{\sim}}{R_{=}} = 2.45$ for the coil for $t = 70 \times 10^{-3}$ sec. $R_{dc} = 0.3$ ohms, which gives $R_{\sim coil} = 0.735$ ohms and $R_{Fe} \cong 10^{-2}$ ohms. See Ref. (4).

TABLE II
MODEL MAGNET MEASURED AND CALCULATED
NON-DIMENSIONAL PARAMETERS^(b)
CALCULATED IN APPENDIX B AND C

	<u>Symbol</u>	<u>Calculated</u>	<u>Measured</u>
Length	ℓ	$\frac{1}{10}$	$\frac{1}{10}$
Number of turns	N	$\frac{300}{330} = \frac{1}{1.1}$	$\frac{1}{1.1}$
Voltage	V	$\frac{1}{1.1}$	$\frac{1}{1.135}$
Time	$t = N\ell^2 V^{-1}$	0.827×10^{-2}	$1.75 \times 10^{-2(a)}$
Magnetic flux density	B	1	1
Magnetic intensity	H	1	1
Permeability	μ	1	1
Total flux	$\phi = \ell^2$	$\frac{1}{100}$	$\frac{1}{100}$
Current	$I = \ell N^{-1}$	$\frac{1}{9.09}$	$\frac{1}{9.14}$
Ampere-turns	$NI = \ell$	$\frac{1}{10}$	$\frac{1}{10.35}$
Resistance	$R = \ell t^{-1} N^2$	10	16
Inductance	$L = \ell N^2$	$\frac{1}{12.1}$	$\frac{1}{13}$
Capacitance	$C = \ell^{-1} N^{-2} t^2$	8.3×10^{-4}	3.6×10^{-3}

(a) The time has to be taken at maximum current.

(b) ℓ , N, V etc. represent reduction ratios of the model to the actual magnet.

In Eq. (1) the same values of α and λ were assumed for both coil sections to ease coil manufacturing.

The values of α , β_1 and β_2 can be calculated from the following considerations:

a. The field contribution due to the core structure (Fig. 1) is asymmetric with respect to the midplane. The magnetic field due to the coil MMF should compensate for this deficiency.

b. The power requirement for a given central field and axial coil spacing must be a minimum. Hence,

$$dP = \frac{\partial P}{\partial \alpha} d\alpha + \frac{\partial P}{\partial \beta_1} d\beta_1 + \frac{\partial P}{\partial \beta_2} d\beta_2 = 0 \quad (2)$$

Accordingly, for each coil section,

$$dP_1 = \frac{\partial P_1}{\partial \alpha} d\alpha + \frac{\partial P_1}{\partial \beta_1} d\beta_1 = 0 \quad (3)$$

$$dP_2 = \frac{\partial P_2}{\partial \alpha} d\alpha + \frac{\partial P_2}{\partial \beta_2} d\beta_2 = 0 \quad (4)$$

with the total power

$$P = P_1 + P_2 \quad (5)$$

The field at the center of each individual coil section due to coil section alone is expressed as

$$B_i = G_i \cdot \left(\frac{P_i \cdot \lambda}{a_i \rho} \right)^{\frac{1}{2}} \quad (6)$$

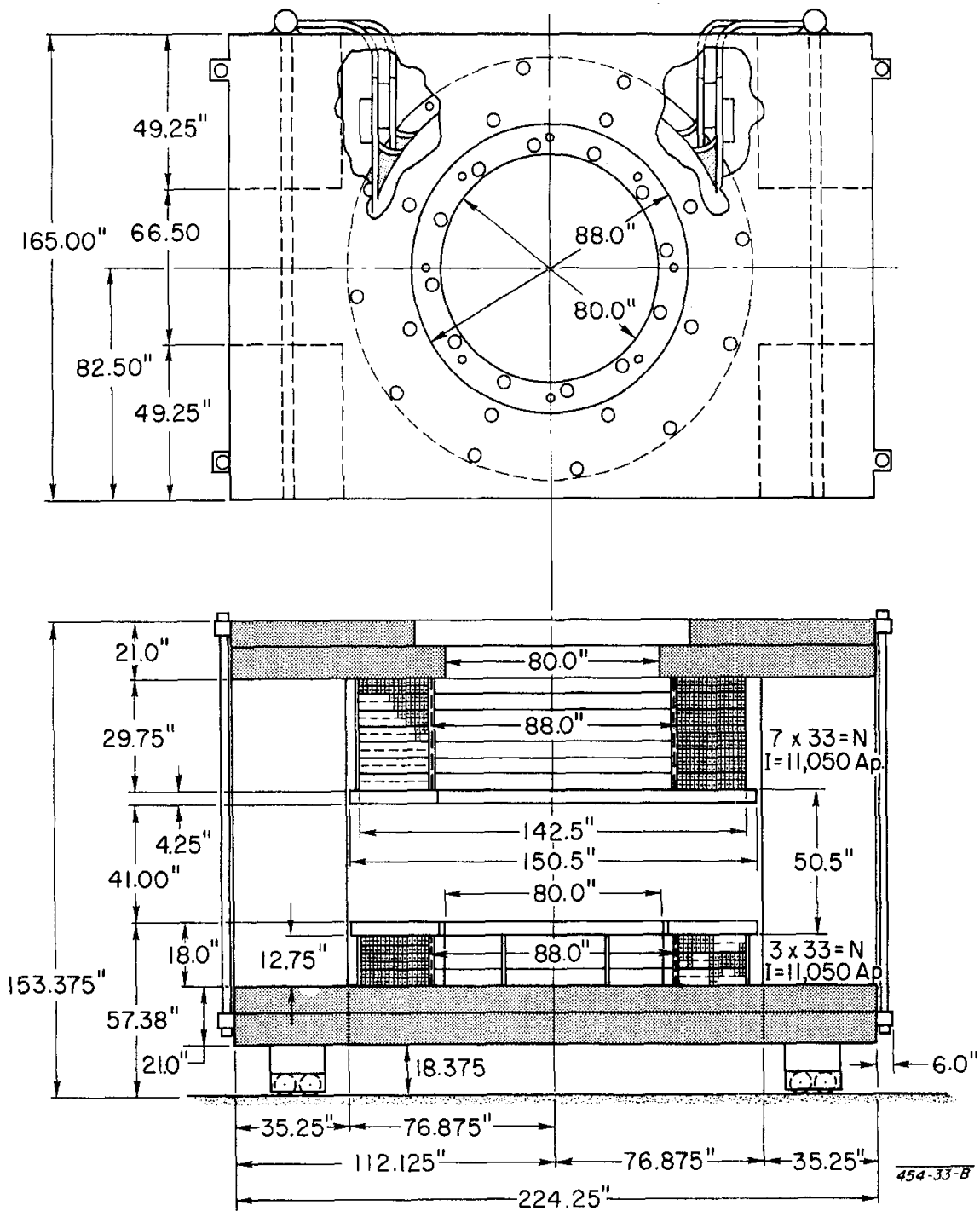


Fig. 1--2-m spark chamber magnet.

with

$$G_i = \frac{1}{5} \left(\frac{2\pi\beta_i}{\alpha^2 - 1} \right)^{\frac{1}{2}} \cdot \ln \frac{\alpha + (\alpha^2 + \beta_i^2)^{\frac{1}{2}}}{1 + (1 + \beta_i^2)^{\frac{1}{2}}} \quad (7)$$

$$i = 1; 2, 3 \dots$$

and is called the geometry or Fabry factor⁶ for constant current distribution.

Geometry factors for various values of α and β are given in Fig. 2. For the 2-meter spark chamber magnet (see Fig. 1 and Table I) the magnet parameters are calculated and given in Table III.

B. Iron Shell

The field contribution due to the iron shell around the coils to the field due to the coil MMF is generated from the aligned dipoles in the iron. The maximum contribution is obtained when all the iron is saturated.

In early calculations^{5,6} it was assumed that the iron magnetization $4\pi M$ is constant. The field components for the axial symmetric case is given by:

$$B_z = \frac{M}{4\pi} \int_{\psi_2}^{\psi_1} \left[(2z^2 - l^2) \cdot \cos \theta - 3zl \sin \theta \right] \frac{Y \cdot A \cdot B}{x^5} d\psi \quad (8)$$

$$B_r = \frac{M}{4\pi} \int_{\psi_2}^{\psi_1} \left[(2l - z^2) \cdot \sin \theta - 3zl \cdot \cos \theta \right] \frac{Y \cdot A \cdot B}{x^5 l} \cdot (Y \cdot \cos v - r) d\psi \quad (9)$$

Figure 3 illustrates the rotations and the coordinates of an iron cube in space with the sides A and B.

The assumption of uniform magnetization in iron leads to errors in excess of 10% in the gap.

The more accurate calculation is based on solution of nonlinear quasi-Poisson equations. Using Maxwell's equation,

$$\nabla \times \left(\frac{1}{\mu} \nabla \times \vec{A} \right) = \vec{S} \quad (10)$$

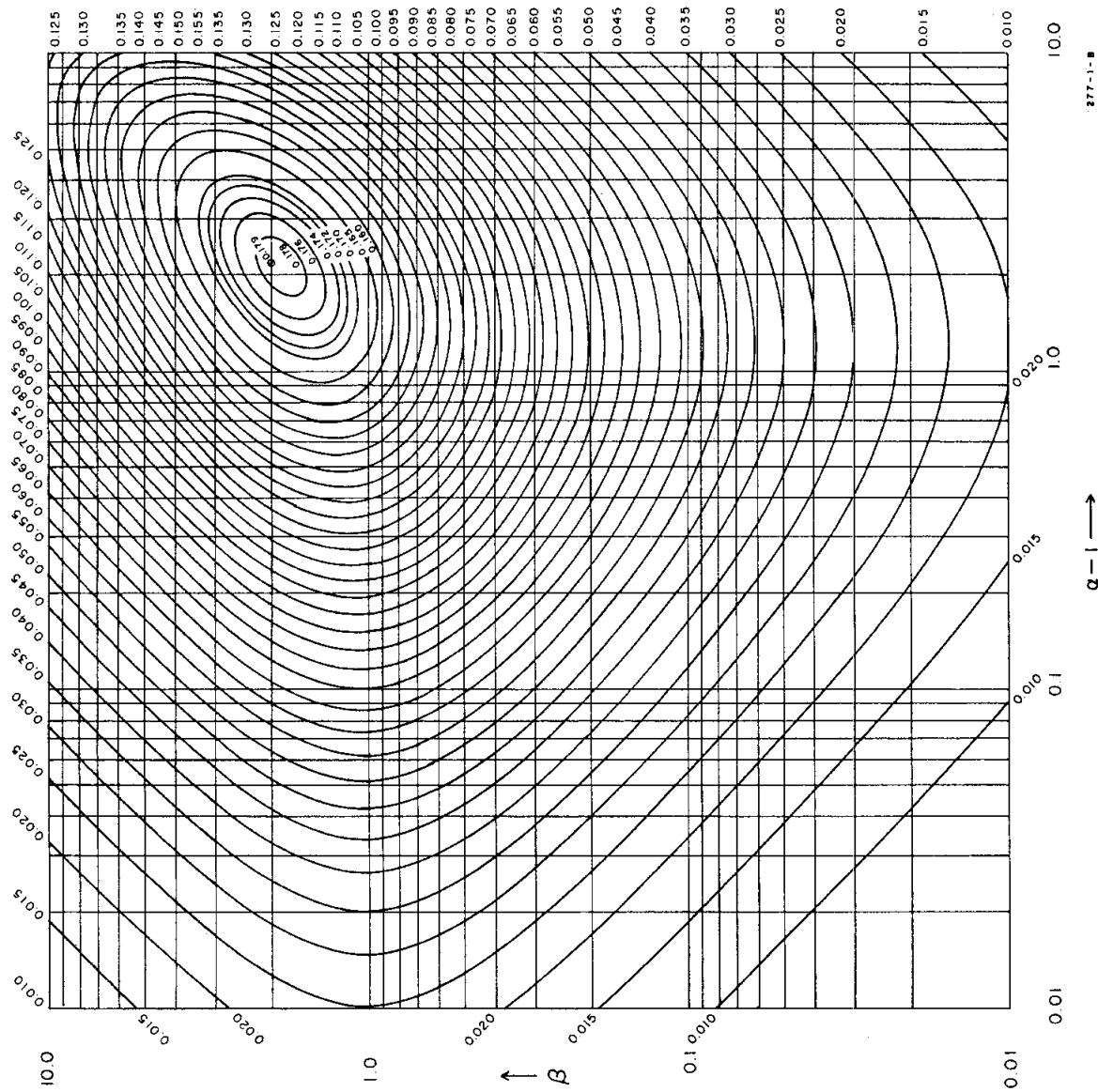
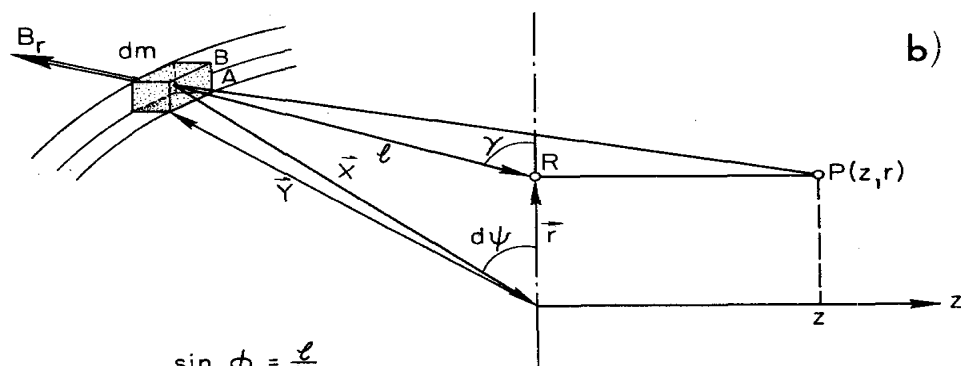
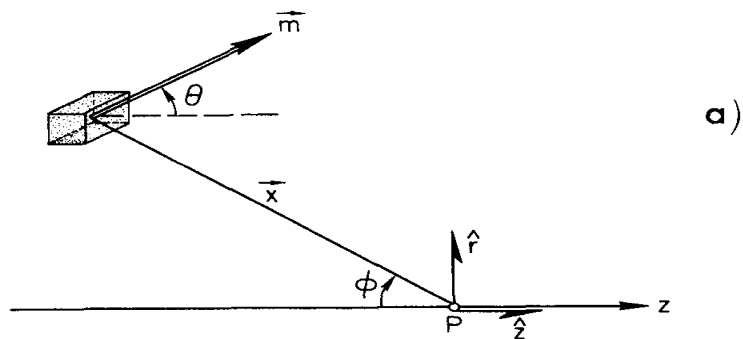


Fig. 2- Geometry factors versus α and β for constant current distribution.

TABLE III

CALCULATED 2-METER SPARK CHAMBER COIL PARAMETER

Inner diameter $2a$ (meters)	2.23
Outer diameter $2a_2$, (meters)	3.61
Gap $2g$ (meters)	1.283
<u>Section I</u> (Top Coil)	
Axial length $2a_1\beta_1$ (meters)	0.7556
Coil center position $a_1 \gamma_1$ (meters)	1.0193
Space factor γ	0.65
Ampere-turns N_1I	2.55×10^6
Turns per double pancake	33
Number of double pancakes	7
Current density (A/cm^2)	837.755
G-factor	0.112
Magnetic field at coil center (kG)	11.88
(Coil I only)	
Power required (MW)	3.87
<u>Section II</u> (Bottom Coil)	
Axial length $2a_1\beta_2$ (meters)	0.318
Coil center position $a_1 \gamma_2$ (meters)	0.8005
Space factor	0.65
Ampere-turns N_2I	1.095×10^6
Turns per double pancake	33
Number of double pancakes	3
Current density (A/cm^2)	837.755
G-factor	0.07
Magnetic field at coil center (kG)	4.85
(Coil II only)	
Power required (MW)	1.66
Field at the center of the coil system without iron (kG)	9.7



$$\sin \phi = \frac{\ell}{x}$$

$$\cos \phi = \frac{z}{x}$$

$$\cos \gamma = \frac{Y \cdot \cos \phi - r}{\ell}$$

$$dm = A \cdot B \cdot Y d\phi \cdot M$$

= DIPOLE DIFFERENTIAL VOLUME

346-12-A

Fig. 3--Magnetic dipole configuration.

we get for two-dimensional configurations (A independent of z component):

$$\frac{\partial}{\partial z} \left(\frac{1}{\mu} \frac{\partial Az}{\partial x} \right) = \frac{\partial}{\partial z} \left(\frac{1}{\mu} \frac{\partial Az}{\partial y} \right) = 0$$

and obtain

$$\frac{\partial}{\partial x} \left(\frac{1}{\mu} \frac{\partial Az}{\partial x} \right) + \frac{\partial}{\partial y} \left(\frac{1}{\mu} \frac{\partial Az}{\partial y} \right) = -S \quad (11)$$

which is the quasi-Poisson equation for magnetic vector potential. The permeability μ and vector potential A are functions of the iron saturation and therefore dependent on the x, y coordinates in a Cartesian system or the r, z coordinate in an axial symmetric system. Equation (10) in cylindrical coordinates is written² (A is independent of the θ component) as

$$\frac{\partial}{\partial r} \left[\frac{1}{\mu r} \frac{\partial}{\partial r} (r A_\theta) \right] + \frac{\partial}{\partial z} \left[\frac{1}{\mu r} \frac{\partial}{\partial z} (r A_\theta) \right] = -S \quad (12)$$

The iron is divided into blocks of reasonable size with the side length $2h$ small enough that we may assume the permeability μ in each block to be constant. We can rewrite Eq. (12) for axial symmetric cases in terms of a difference equation:

$$A_o = \frac{\left(\frac{1}{\mu_1 r_1} + \frac{1}{\mu_o r_o} \right) r_1 A_1 + \left(\frac{1}{\mu_2 r_2} + \frac{1}{\mu_o r_o} \right) r_2 A_2 + \left(\frac{1}{\mu_3 r_3} + \frac{1}{\mu_o r_o} \right) r_3 A_3 + \left(\frac{1}{\mu_4 r_4} + \frac{1}{\mu_o r_o} \right) r_4 A_4 + 2h^2 S_o}{r_o \left(\frac{1}{\mu_1 r_1} + \frac{1}{\mu_2 r_2} + \frac{1}{\mu_3 r_3} + \frac{1}{\mu_4 r_4} + \frac{1}{\mu_o r_o} \right)} \quad (13)$$

and the field intensity in cylindrical coordinates:

$$\vec{H} = -\frac{1}{2\mu_o} \cdot \left(\frac{A_3 - A_4}{h} \right) \hat{e}_1 + \frac{1}{\mu_o} \left(\frac{A_1 - A_2}{h} \right) \hat{e}_3 \quad (14)$$

The notations used are accordingly:

$$\begin{aligned}A_{\theta}(r, z) &= A_0 \\A_{\theta}(r + h, z) &= A_1 \\A_{\theta}(r - h, z) &= A_2 \\A_{\theta}(r, z + h) &= A_3 \\A_{\theta}(r, z - h) &= A_4\end{aligned}$$

The "Nutcracker" Program² calculation is based on Eqs. (13) and (14) and an overrelaxation method. It computes the field due to the coil and iterates the field in the iron until the change is less than 5% due to all iron blocks.

The field distribution $B = f(R, 0)$ in the median plane and $B_z = f(z, 0)$ are shown in Figs. 4 and 5. The radial field component is illustrated in Fig. 6.

In the calculation the rectangular shape of the horizontal yoke was converted into a cylinder of the same total cross section and axial height. The four vertical yokes were changed into one iron shell surrounding the coils. The determination of its exact location in the radial direction around the coil is difficult and crude assumptions affecting the field distribution had to be made. The shape of the fringing field and its radial and axial distribution, therefore, do not comply with the actual model measurements. Field comparisons between measurements and calculations are dealt with in Section IV of this report.

The axial field at the median plane is calculated to be 14.6 kG and is about 5% lower than the measured value. This close agreement was achieved after several geometries for calculations were tried out. However, the radial distribution of $B_z = f(R)$ does not agree fully with the measured data. The rapid fall-off of B_z is due to the positioning of the vertical yoke, the assumption of field-free boundaries, and is not consistent with measurements. The computer program needs to be expanded for three-dimensional iron configurations in order to give accurate results in the fringing field area.

The calculated radial field component, shown in Fig. 6, is higher than the measured values, which seems strange because of the axial symmetry assumption. This may be the case due to the location of the median plane. The field calculation was performed using a $5 \times 5 \text{ cm}^2$ mesh size over the whole magnet area. By shifting the axial location of the median plane over $\pm 2 \text{ cm}$, the field

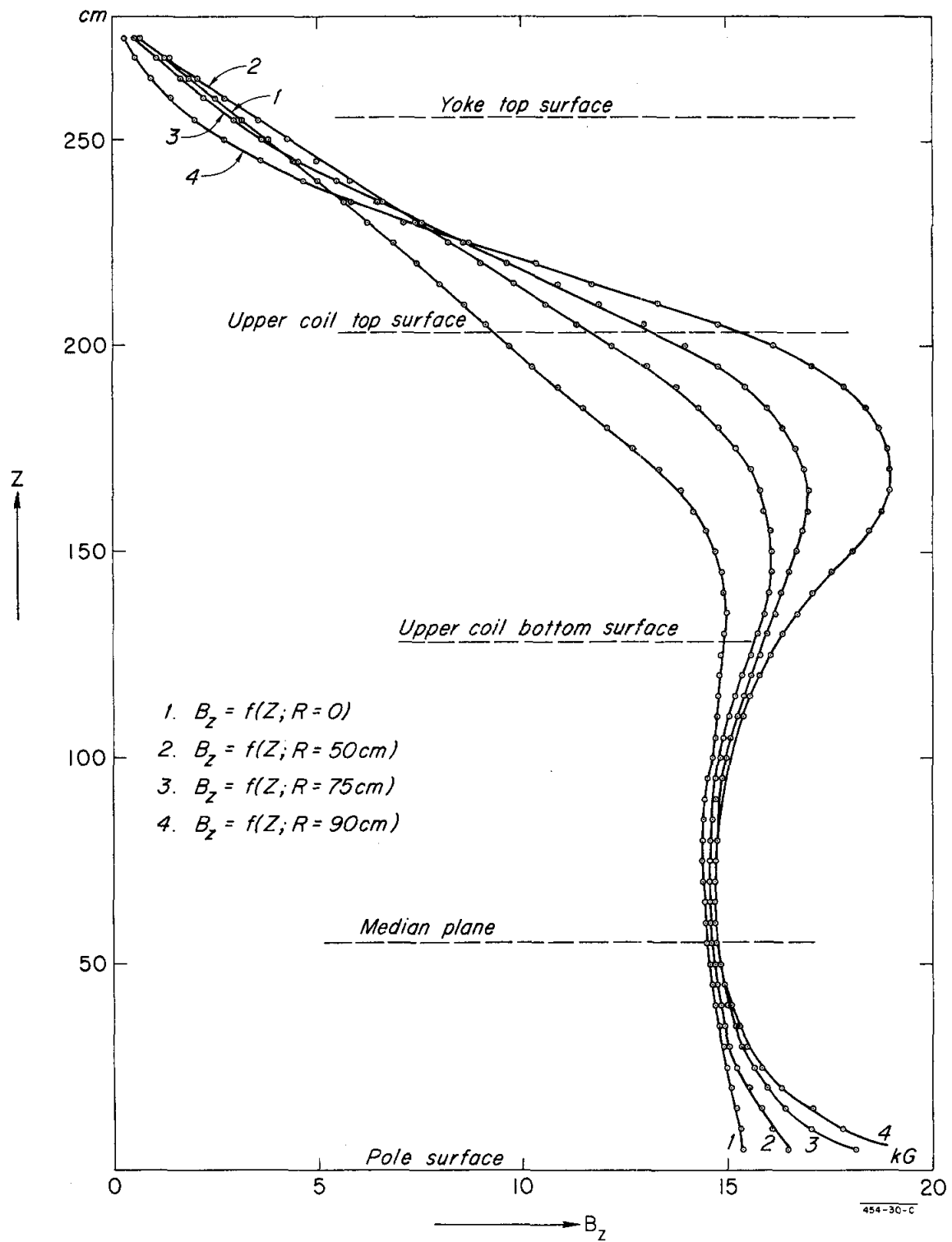


Fig. 4--Calculated axial distribution of the axial magnetic field.

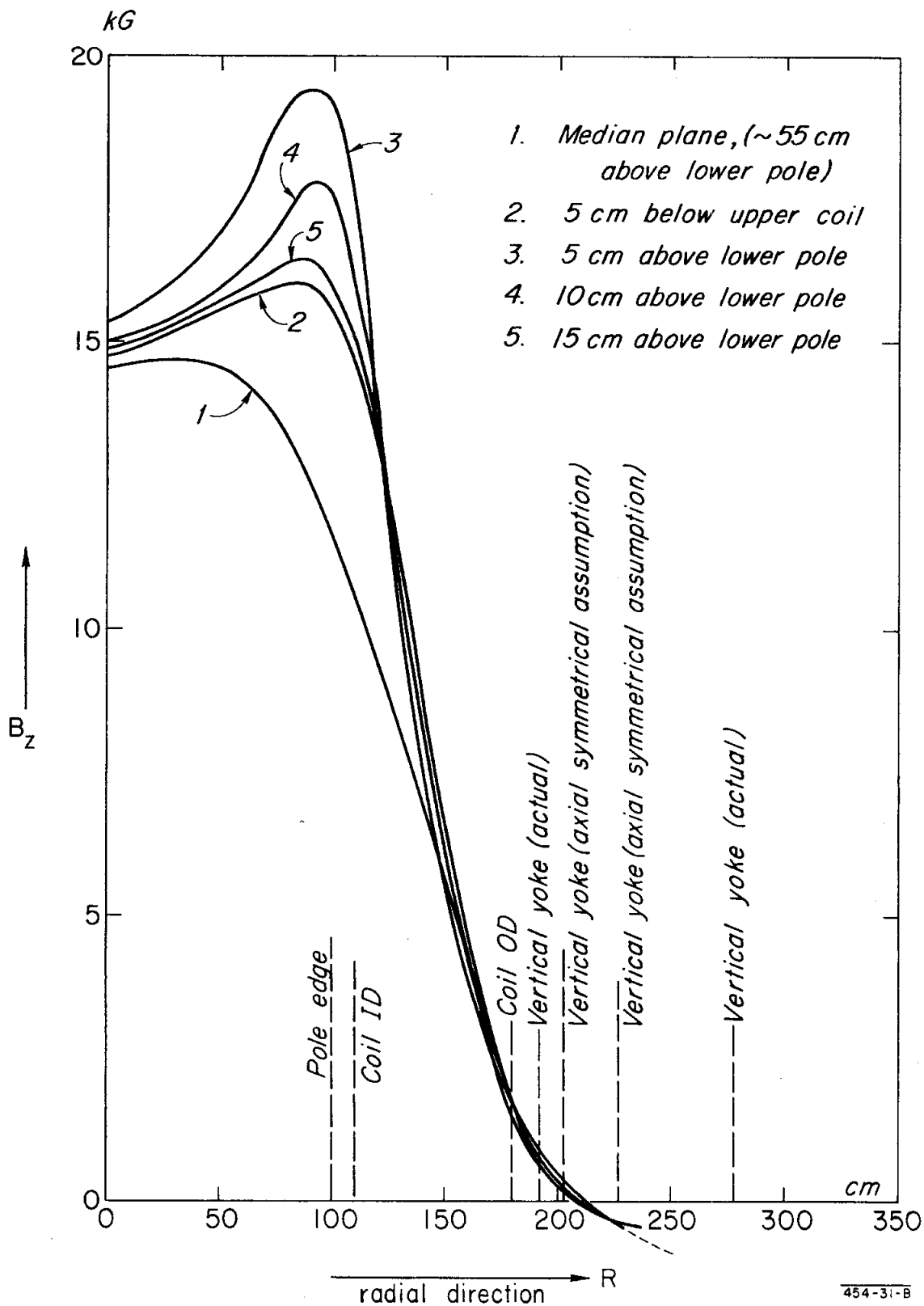


Fig. 5--Calculated radial distribution of the axial magnetic field.

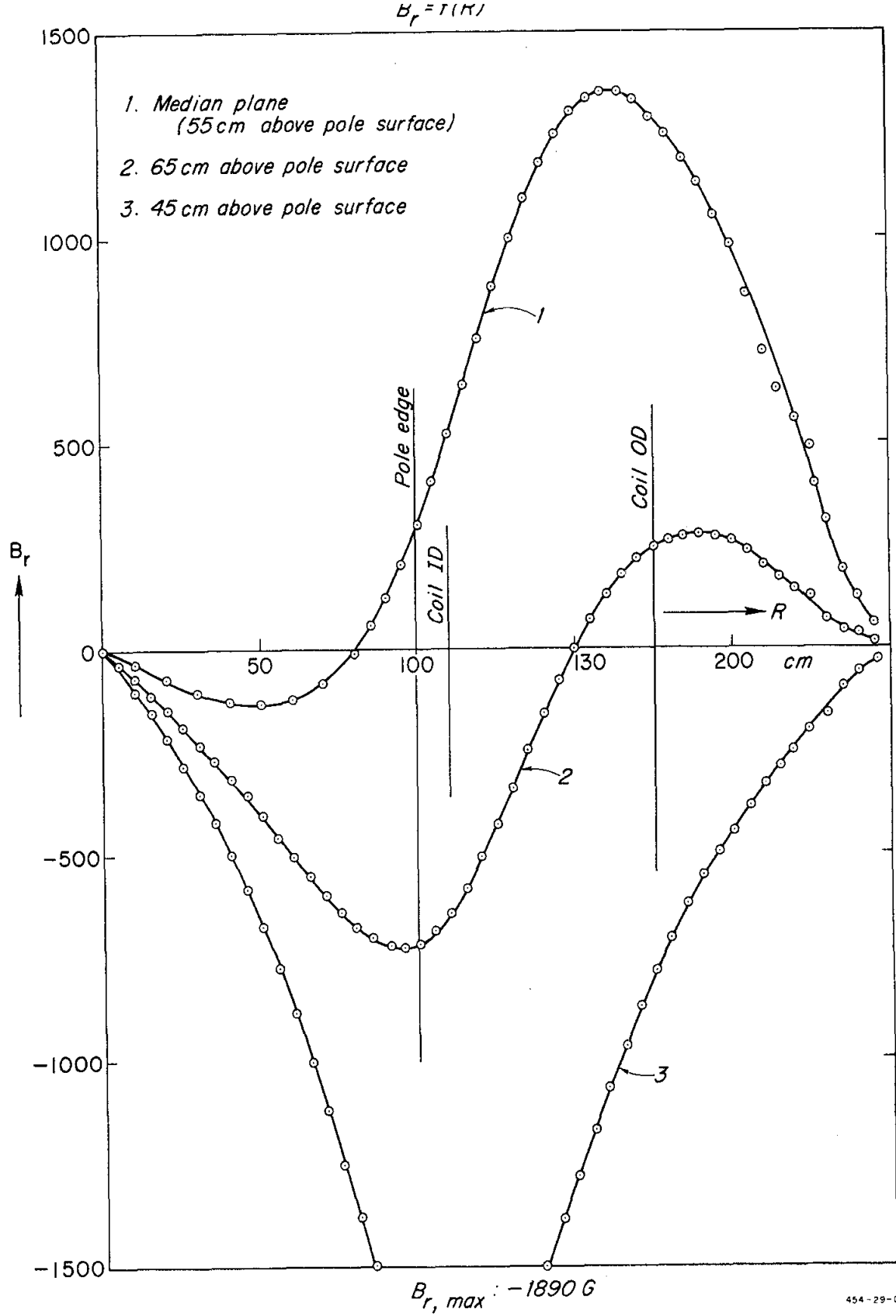


Fig. 6--Radial distribution of the radial field.

radial component changes appreciably; therefore, the actual location of the median plane is between 52 and 56 cm above the pole surface. However, further detailed computation was omitted at this point.

As expected, the iron is saturated only in a few areas. The axial and radial field components inside the iron are shown in Table IV. The pole height is 45.7 cm and pole diameter 203.2 cm. The center of the pole surface is taken as the origin of the coordinate system, z, r . The components of flux density are positive in the direction of positive r and positive z .

C. Forces

The calculation of forces acting on various parts of iron and between iron and coils is based on the energy equation:

$$W = \frac{1}{2} \int_{r_1}^{r_2} \int_{\theta_1}^{\theta_2} \int_{z_1}^{z_2} \vec{H} \cdot \vec{B} \cdot r dr d\theta dz \quad (15)$$

The magnetic energy in a circular iron ring with axial and radial dimensions (h) and constant permeability μ_v in a block v , is derived from Eq. (15):

$$W = \frac{1}{2} \int_{r_{o,v} - \frac{h}{2}}^{r_{o,v} + \frac{h}{2}} \int_{\theta - \frac{d\psi}{2}}^{\theta + \frac{d\psi}{2}} \int_{z - \frac{h}{2}}^{z + \frac{h}{2}} \mu \vec{H}_v \cdot \vec{H}_v r dr d\theta dz \quad (16)$$

where \vec{H}_v is the field intensity at $r_{o,v}$ for a block v .

The force acting on v is:

$$F = \nabla W = \frac{\partial W}{\partial r} \hat{e}_1 + \frac{1}{r} \frac{\partial W}{\partial \theta} \hat{e}_2 + \frac{\partial W}{\partial z} \hat{e}_3 \quad (17)$$

From Eq. (16) we may write:

$$\nabla W = \frac{d\psi}{2} \left(\frac{\partial}{\partial r} \hat{e}_1 + \frac{\partial}{\partial z} \hat{e}_2 \right) \int \int \mu H^2 r dr dz$$

TABLE IV
FIELD DISTRIBUTION IN BOTTOM POLE AND YOKE

z(cm)	Coordinates		B_z (kG)	Remarks
	r(cm)	B_r (kG)		
0	0	0	14.6	Pole Surface
	25	- 6.7	15.7	
	50	- 9.53	16.6	
	75	- 11.9	18.1	
	95	- 14.3	22	
	100	- 17.3	20.4	Pole Edge
5	0	0	20	
	25	- 8.0	20	
	50	- 17.9	18.8	
	75	- 15.5	19.5	
	95	- 16.2	23.27	
	100	- 17.4	19	
10	0	0	21.6	
	25	- 2.75	21.5	
	50	- 7.5	20.5	
	75	- 10.9	21	
	95	- 12.55	24.7	
	100	- 13.9	19.3	
20	0	0	22.9	
	25	- 0.93	23	
	50	- 2.5	23.1	
	75	- 5.55	23.3	
	95	- 7.15	27	
	100	- 8.55	20.7	
30	0	0	23.2	
	25	- 0.46	23.6	
	50	- 0.75	23.8	
	75	- 1.08	24.6	
	95	- 1.7	28.55	
	100	- 1.855	21.9	

TABLE IV - Cont.

Coordinates				Remarks
z(cm)	r(cm)	B _r (kG)	B _z (kG)	
40	0	0	23.3	
	25	0.064	23.5	
	50	1.4	23.6	
	75	2.65	24.2	
	95	5.25	26.6	
	100	1.17	21.5	
45	0	0	23.1	Pole Neck
	25	1.08	23.1	
	50	2.26	23.2	
	75	4.72	23.2	
	95	1.2	21.3	
	100	1.7	20.2	
50	0	0	22.5	Bottom Yoke
	25	1.32	22.6	
	50	3	22.6	
	75	6.95	21.7	
	100	18.7	15	
	125	23.7	8.1	
60	0	0	21.3	
	25	2.02	21.3	
	50	5.36	20.5	
	75	14.2	16	
	100	21.1	10.45	
	125	22.7	6.1	
70	0	0	19.32	
	25	3.5	18.9	
	50	11.5	15.5	
	75	19	11.1	
	100	22.2	7.25	
	125	21.8	4.3	
80	0	0	16.3	
	25	7.04	14.5	

TABLE IV - Cont.

Coordinates				Remarks
z(cm)	r(cm)	B _r (kG)	B _z (kG)	
90	50	16.95	9.32	
	75	21.2	7.14	
	100	23	4.57	
	125	23.2	2.55	
	0	0	8.4	
	25	14.8	5.35	
	50	20.2	4.01	
	75	22.7	3.65	
	100	24.1	2.15	
	125	24.06	0.86	
100	0	0	0.68	Yoke Bottom
	25	9.02	0.19	
	50	12.5	0.62	
	75	14.5	1.37	
	100	16.05	0.64	
	125	15.7	- 0.76	

which gives the two force components for the axial symmetric case:

$$F_r = \frac{1}{2} \int_0^{2\pi} (\cos \psi + \sin \psi) d\psi \int_{r_{o,v}-\frac{h}{2}}^{r_{o,v}+\frac{h}{2}} \int_{z_{o,v}-\frac{h}{2}}^{z_{o,v}+\frac{h}{2}} \mu H_v H_v r dr dz = 0 \quad (18)$$

$$F_z = \pi \int_{r_{o,v}-\frac{h}{2}}^{r_{o,v}+\frac{h}{2}} \mu \left[\left(\frac{\partial A}{\partial z} \right)^2 + \frac{1}{r^2} \left(\frac{\partial}{\partial r} (rA) \right)^2 \right] r dr \left| \begin{matrix} z_{o,v}+\frac{h}{2} \\ z_{o,v}-\frac{h}{2} \end{matrix} \right. \quad (19)$$

The F_z components of the forces calculated from Eq. (19) are given in Table V.

TABLE V
AXIAL FORCE DISTRIBUTION

Upper horizontal yoke and vertical yokes	1.5×10^7	Newtons
Lower horizontal yoke and vertical yokes	1.7×10^7	Newtons
Upper coil to upper yoke	1.1×10^7	Newtons
Lower coil to lower yoke	6×10^6	Newtons
Upper and lower coil	13×10^4	Newtons

III. THE ELECTROMAGNETIC MODEL

The main purpose of building a 1/10-scale electromagnetic model was to measure axial and radial field components at any point in space using different geometries. The model shown in Fig. 7 is built for pulse operation and is energized from a 60-kilojoule, 5-kilovolt capacitor bank. The core is built from 0.35-mm-thick, grain-oriented silicon sheets, type USS-M6. The magnetization curve of these sheets is given in Fig. 8, where it is compared to the curve for the low carbon steel ($C = 0.05\%$) used for the 2-meter spark chamber magnet. The laminations are glued together by means of a hot setting epoxy. The space factor in the yokes is about 93% and in the poles about 82%.

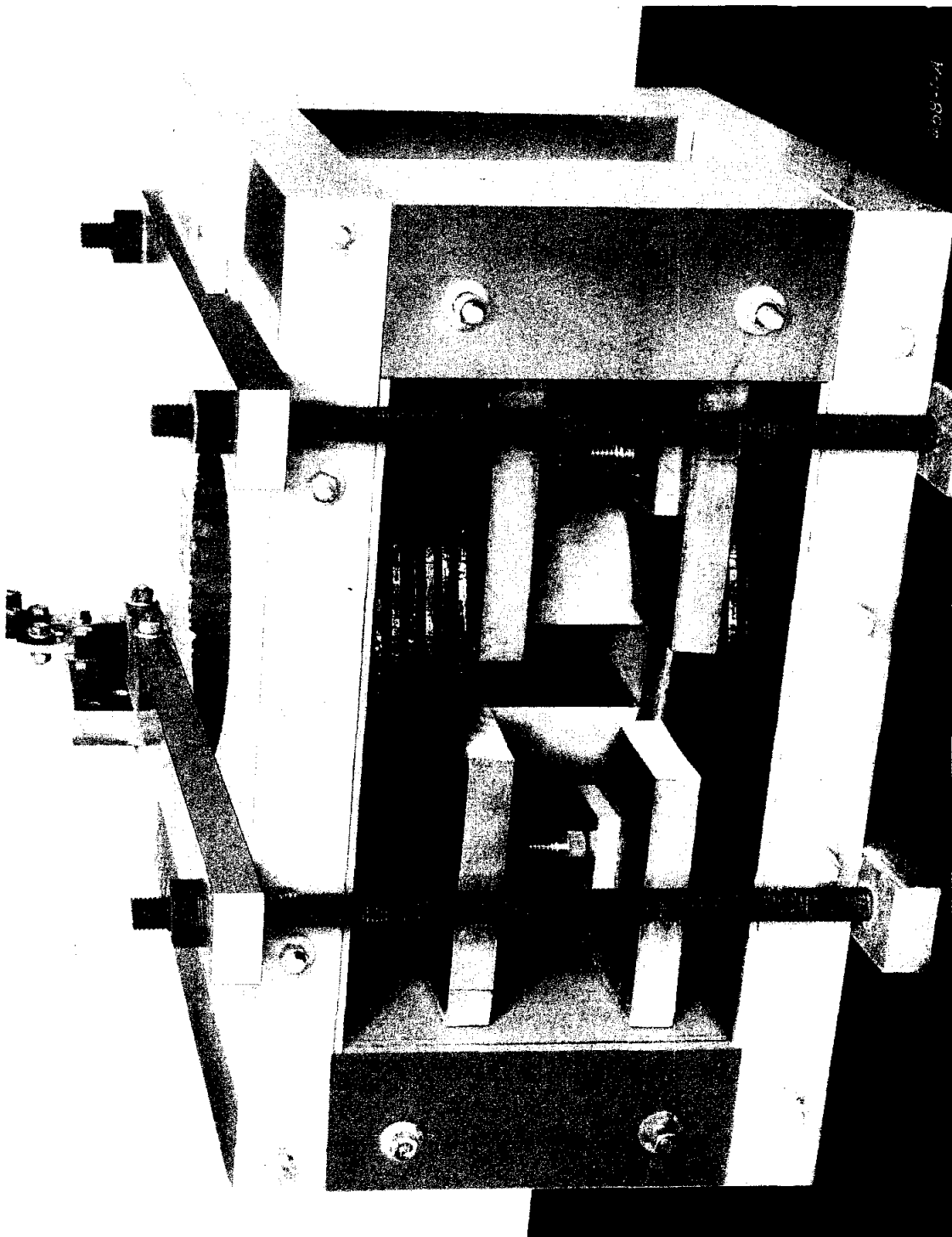
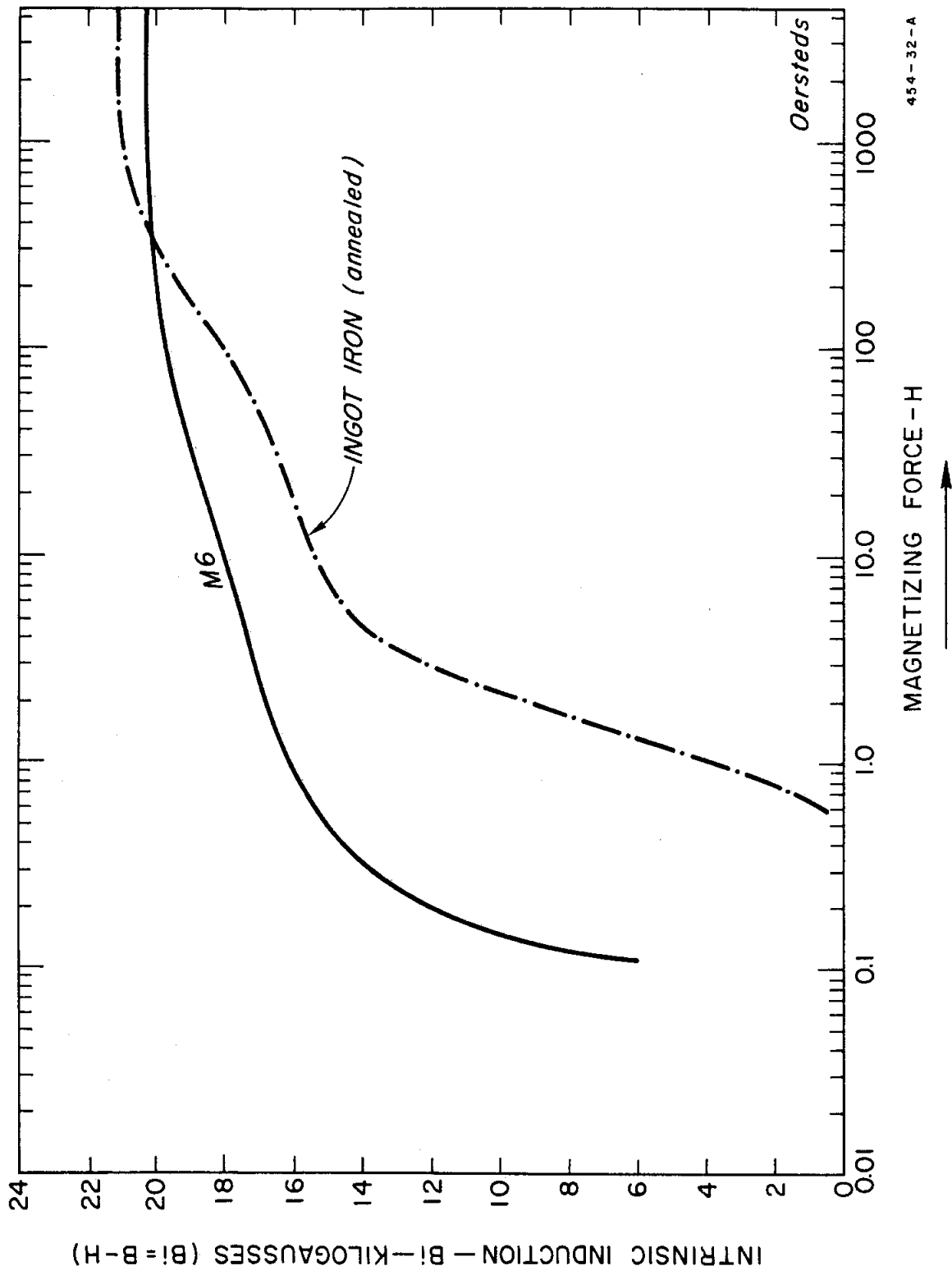


Fig. 7--1/10 scale spark chamber magnet model.



454-32-A

Fig. 8--Magnetization curves of M-6 cold reduced silicon iron and low carbon ingot iron.

The coils are built of enamel-coated square copper conductors, gauge 6. No iron bolts are used. The through bolts are built of pressed and impregnated wood sheets known under the commercial name of Permali. The model can be used in various configurations, as discussed below.

A. Symmetric Magnet

Top and bottom poles were installed. The turn-per-pole number was chosen to be 210, with seven double pancakes around each pole. With a current of $I = 890$ amps, the ampere-turns correspond to 1/10 of that for the 2-meter magnet. No holes are provided in the horizontal yokes (see Fig. 9).

The magnetization curve of the magnet is shown in Fig. 10, Curve I, and is compared to the BI curves of the other cases described below. At a current of 910 amps (equivalent to 382×10^5 ampere-turns, corresponding to 11,510 amps in the 2-meter spark chamber magnet), the field in the center of the gap P ($x = 0$, $y = 0$, $z = 5.58$ cm above pole face) is 22,300 gauss.

The B_z component of the field in the midplane along the x and y direction is illustrated in Figs. 11 and 12. The field is rather inhomogeneous and drops from the center to half pole diameter by 7% and at the pole edge by 28%.

The saturation of the vertical yokes is given in Fig. 13. It is readily seen that even at a 1210-amp excitation current (5.08×10^5 ampere-turns) the flux density in the yoke is 18.7 kG, which is below saturation. It was decided to reduce the cross-sectional area of the yokes from 4.06×7 square inches to 4.06×5.5 square inches, which reduces the peak field in the magnet center from 22.3 kG to 22.0 kG (3.82×10^5 ampere-turns).

The field distribution (B_z) in various planes perpendicular to the pole surfaces and measured at 2.14×10^5 ampere-turns is given in Fig. 14. The magnet inductance is illustrated in Fig. 15.

B. Model with Lower Pole Only

The top pole was removed. In order to compensate for the axial field contribution due to the bottom pole, the upper coil was provided with 8 double pancakes and the lower coil around the pole with 6 double pancakes, each with 30 turns. The yokes remain unchanged (Fig. 16). The B_z field component versus the y coordinate in the geometrical center plane (2 inches above the pole surface) in the gap is illustrated in Fig. 17 for various currents. The magnet inductance is illustrated in Fig. 18.

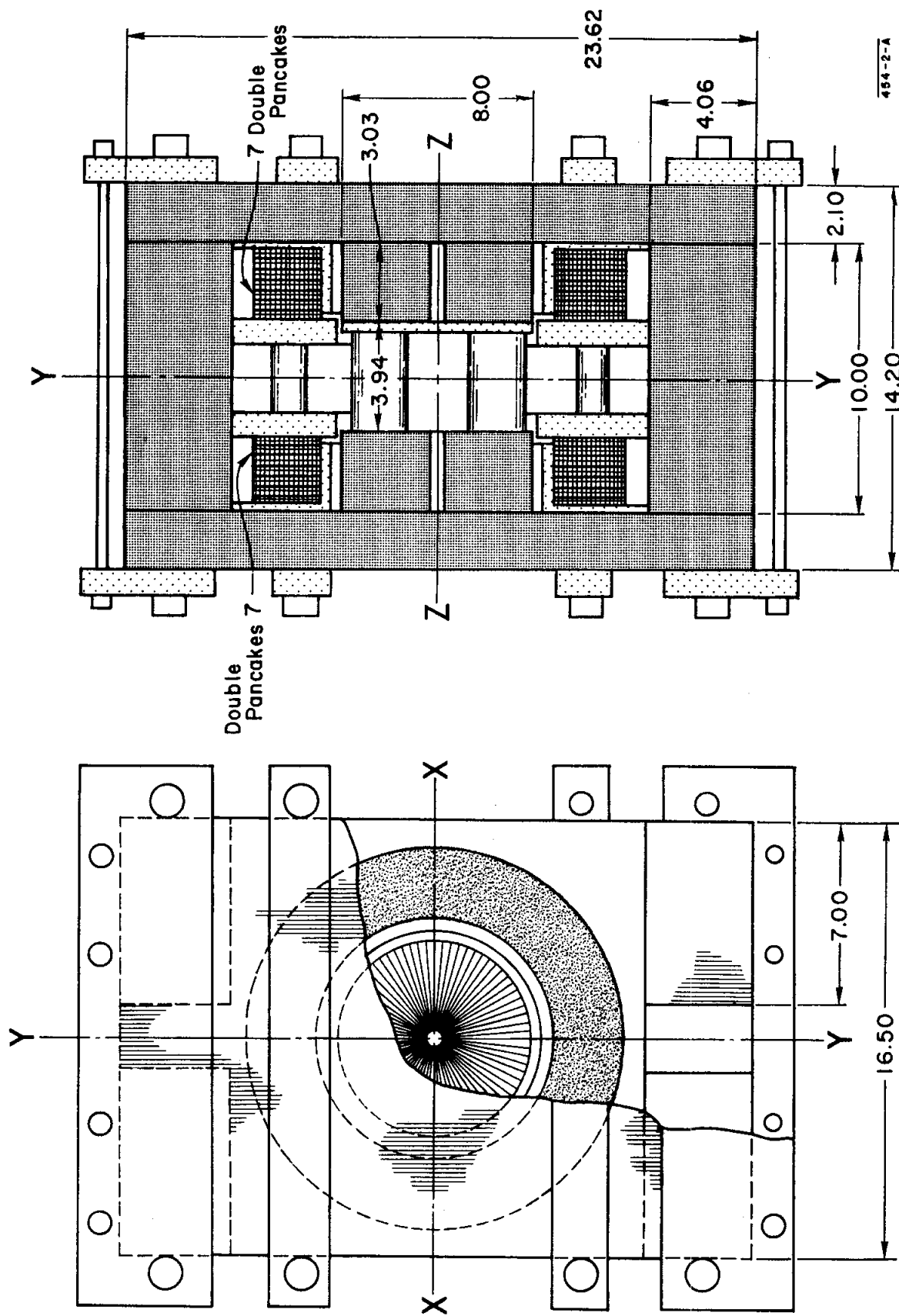


Fig. 9--1/10 scale spark chamber symmetric magnet model with 14 double pancakes.

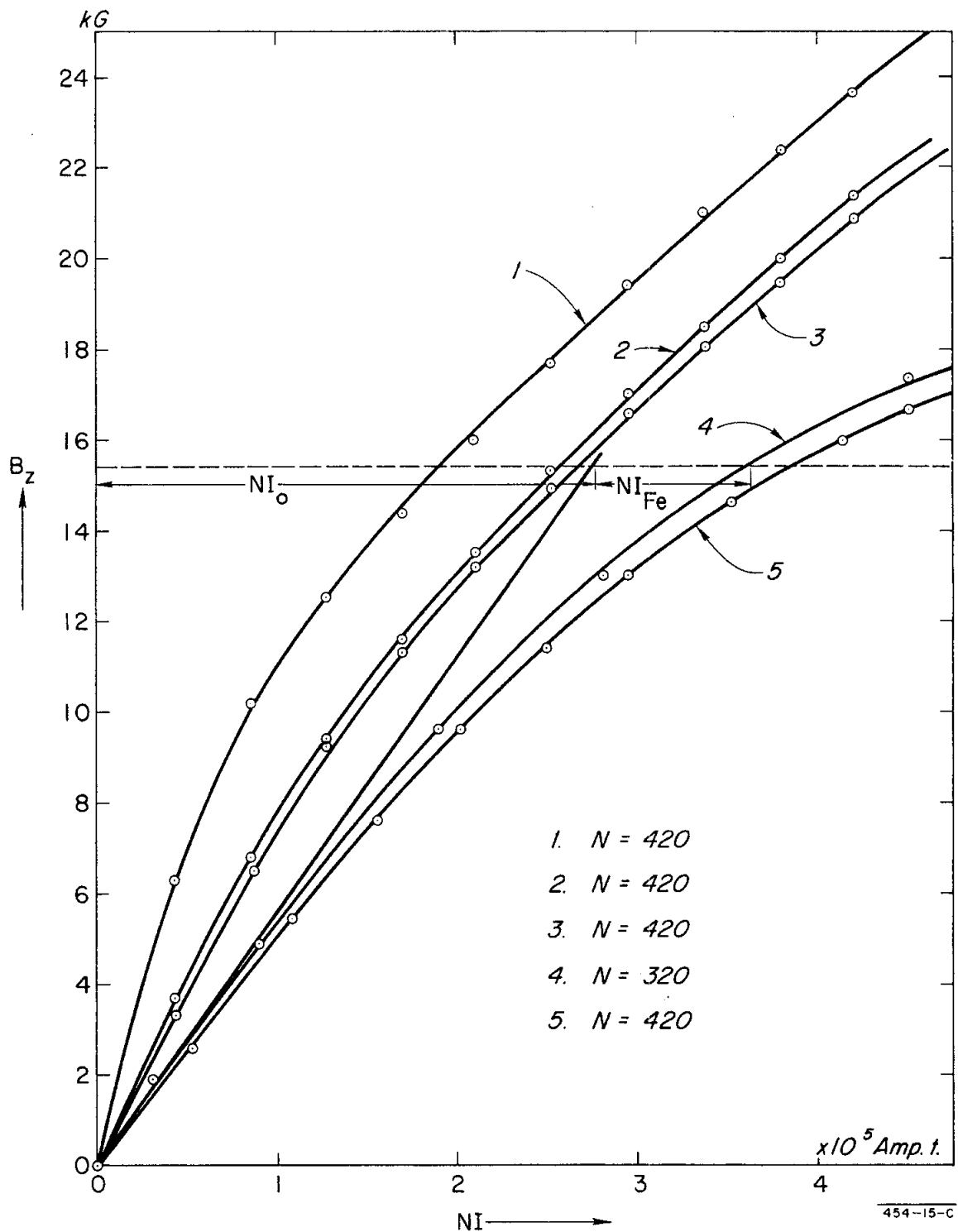


Fig. 10--Magnetization curves of different model magnet configurations.

1. BI curve for symmetric magnet shown in Figure 9
2. BI curve for magnet illustrated in Figure 16
3. BI curve for magnet according to Figure 19
4. BI curve for magnet according to Figure 23 and true replica of the 2-m spark chamber magnet
5. BI curve for magnet according to Figure 23, but distance between upper and lower horizontal yoke unchanged from Fig. 19

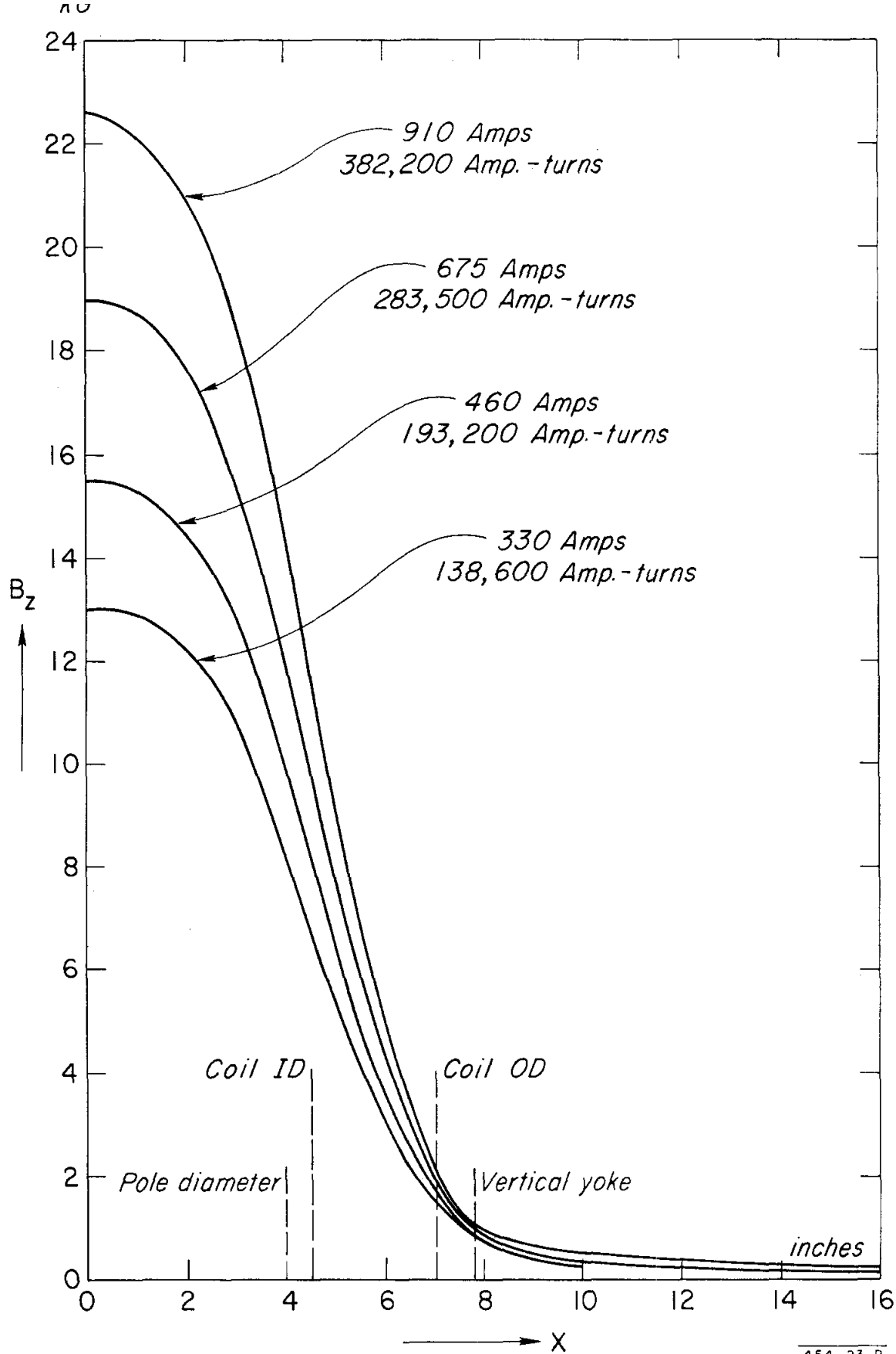


Fig. 11-- B_z distribution along the X axis for variations excitation levels for the symmetric model magnet.

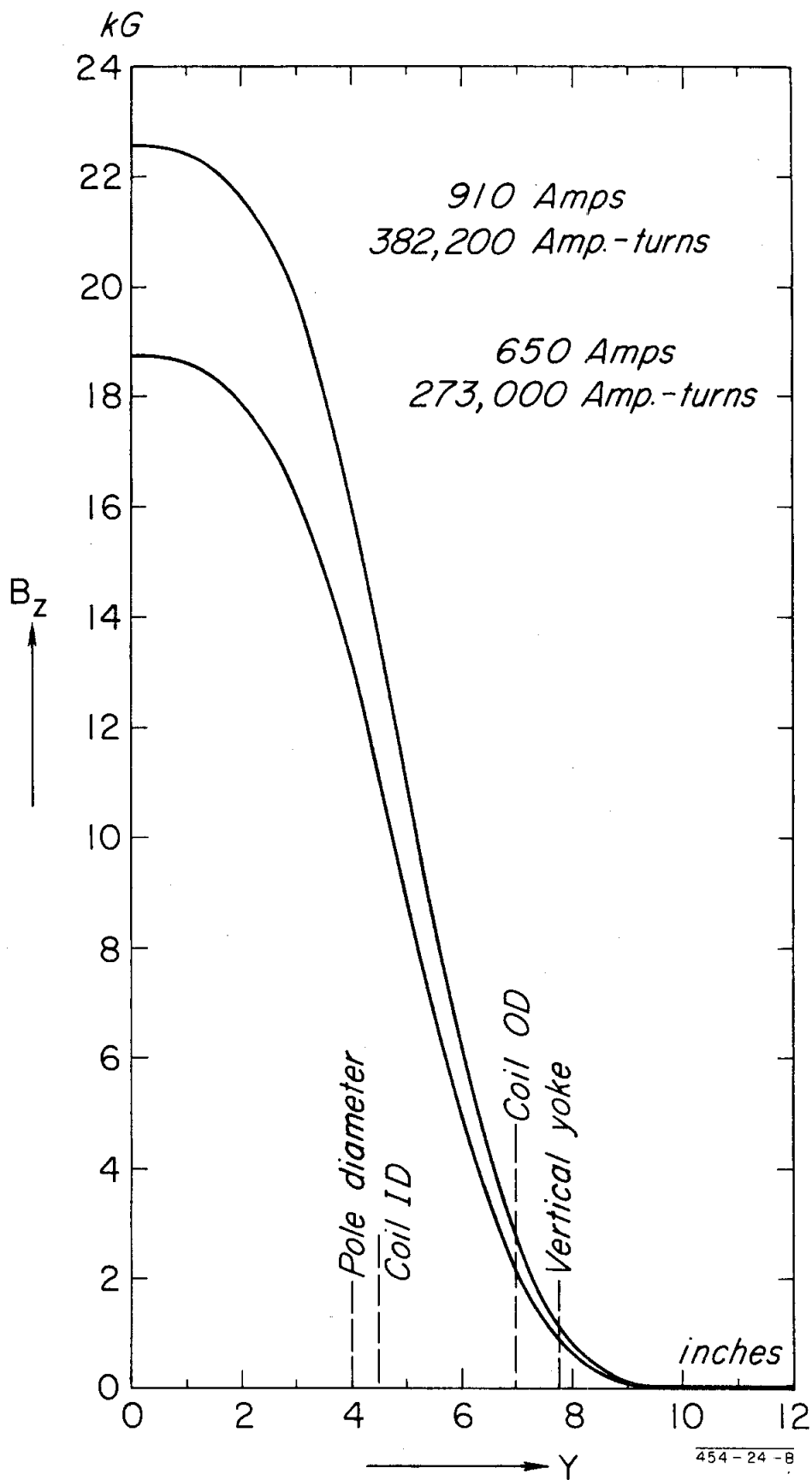


Fig. 12-- B_z distribution along the Y axis for the symmetric model magnet .

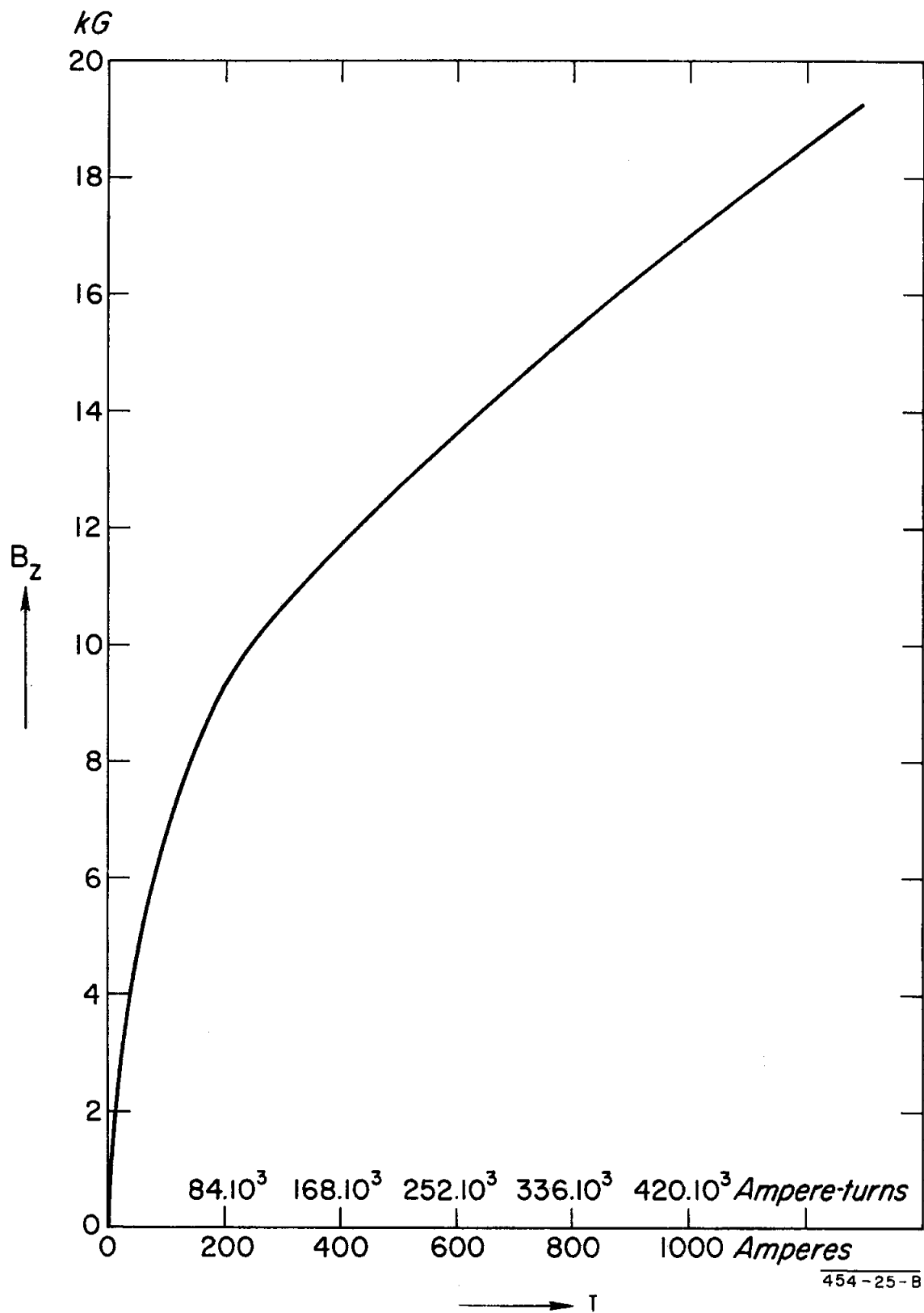


Fig. 13--Saturation curve of the vertical yoke (symmetric model Fig. 9).

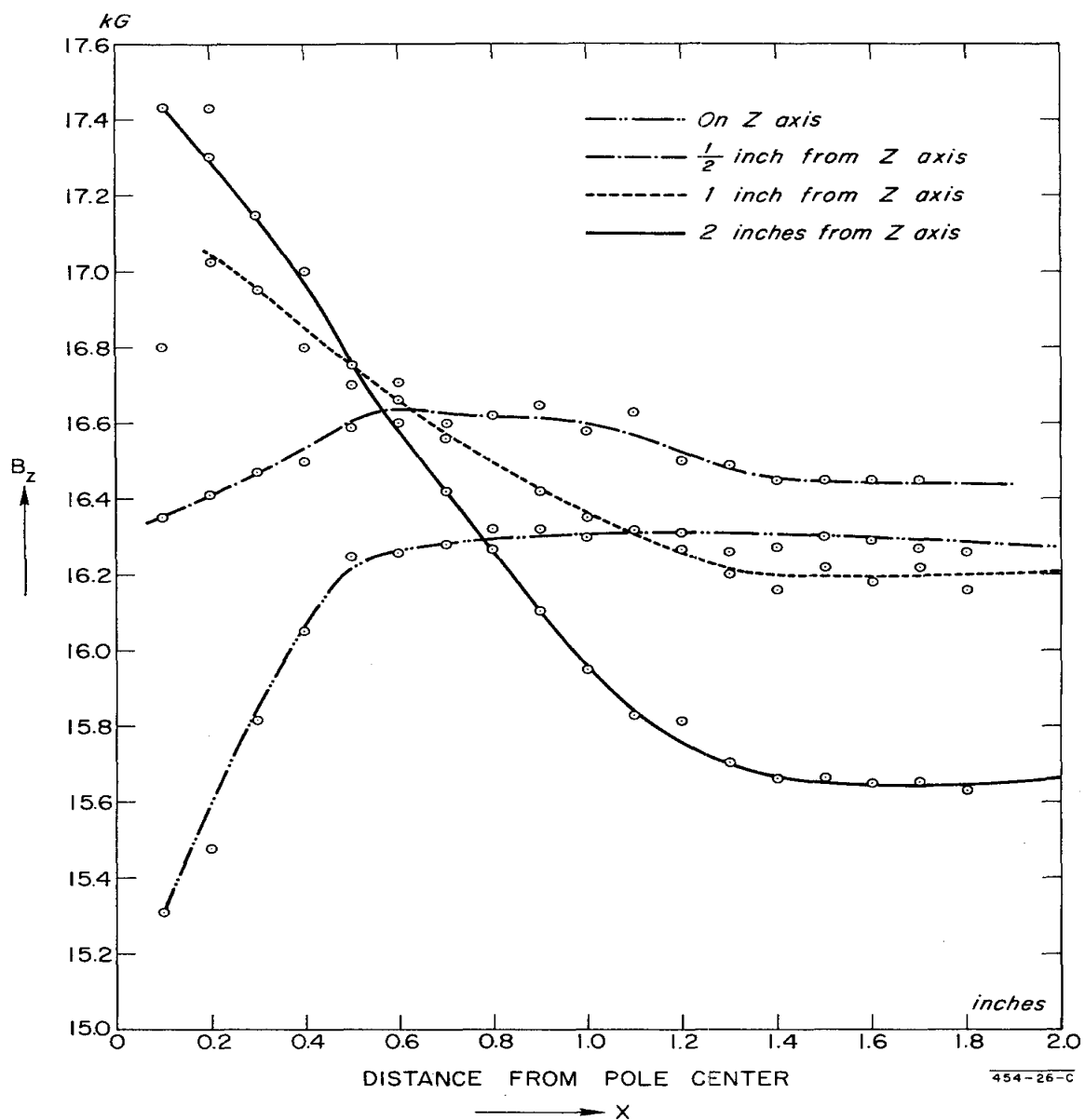


Fig. 14-- B_z distribution in different planes parallel to the pole surface (symmetric model Fig. 9).

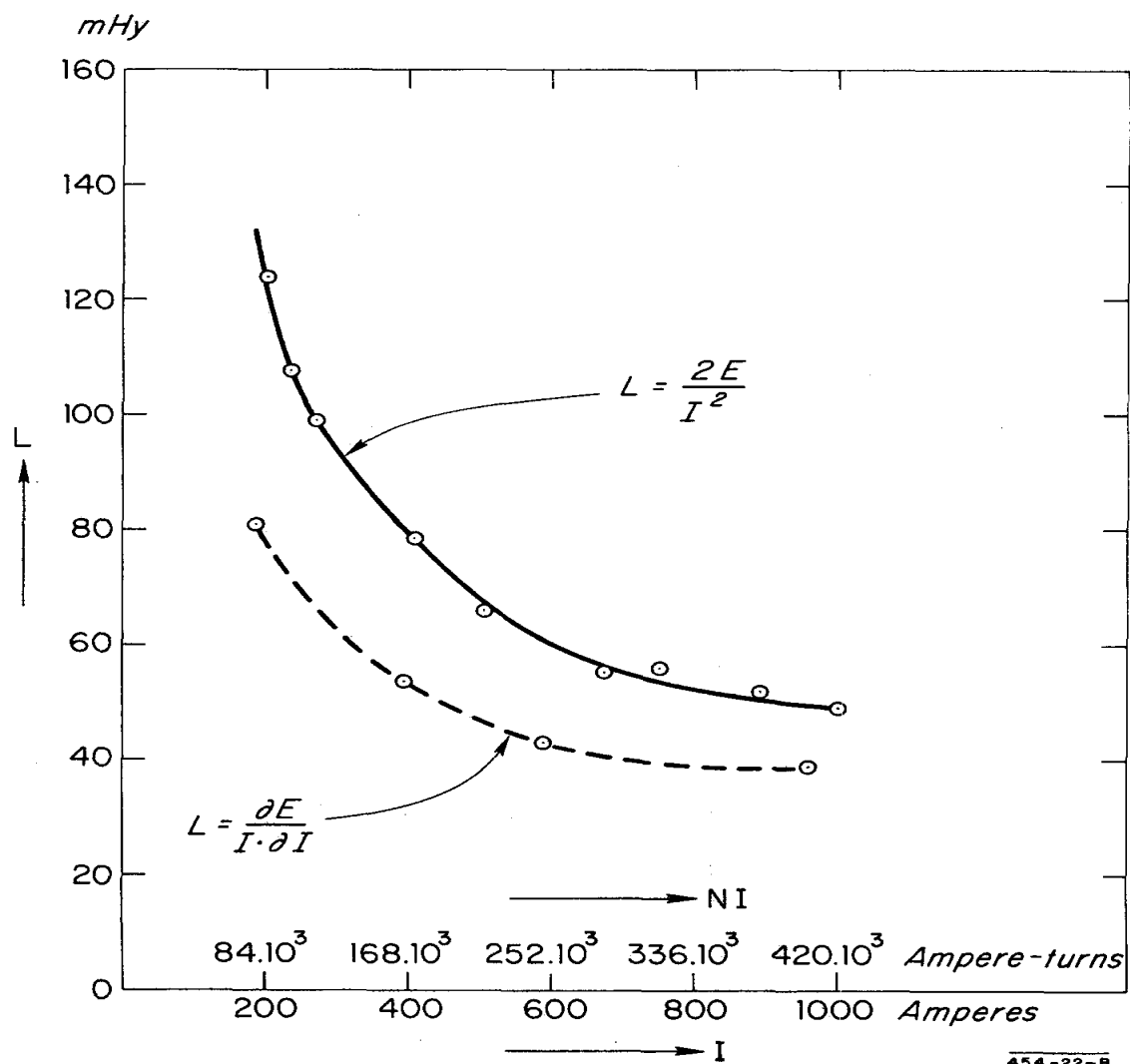


Fig. 15--Inductance versus current (symmetric model Fig. 9).

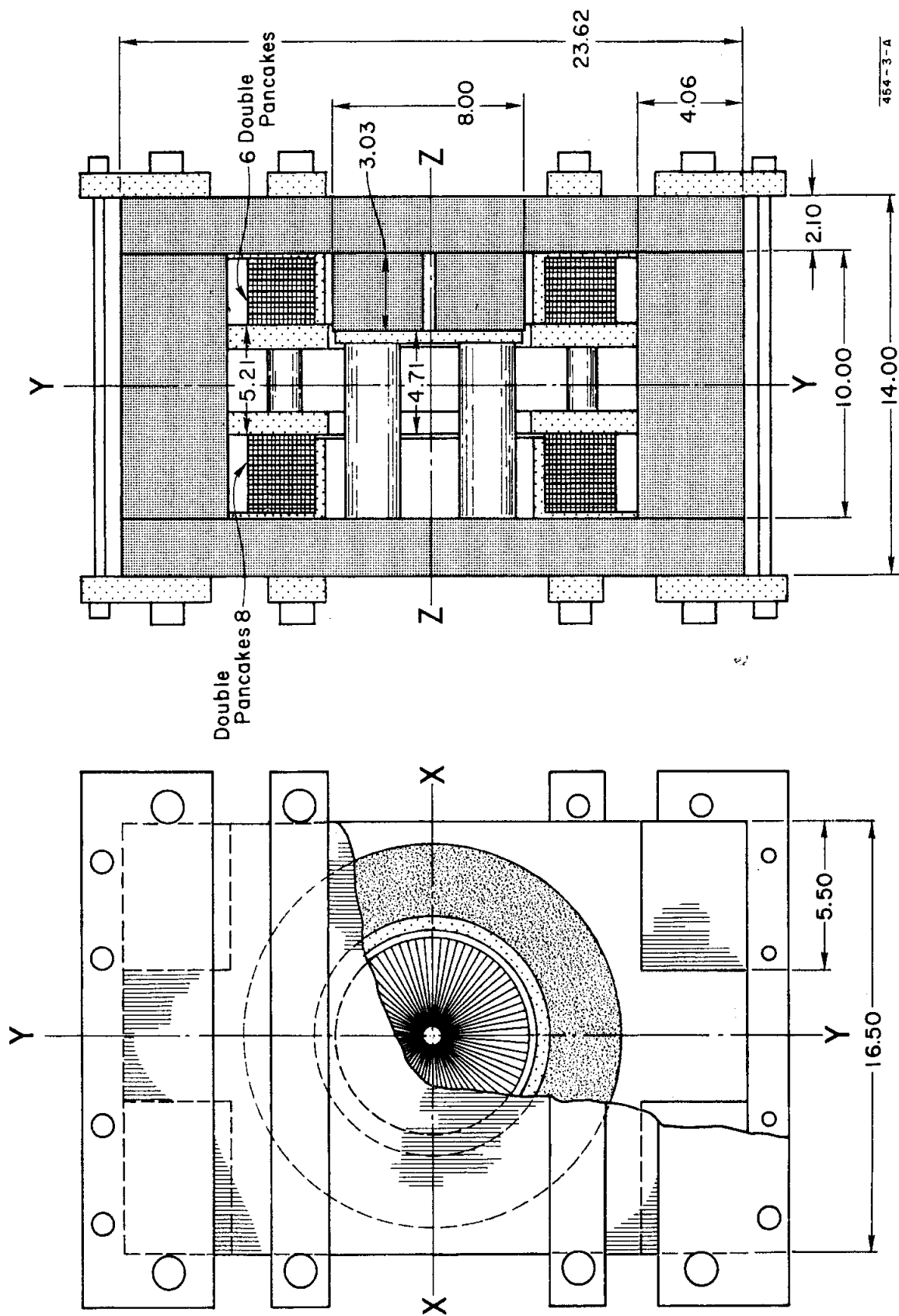


Fig. 16---Asymmetric 1/10 scale model magnet. Upper pole removed. Coils adjusted to compensate for the iron asymmetric configuration. Number of double pancakes 14.

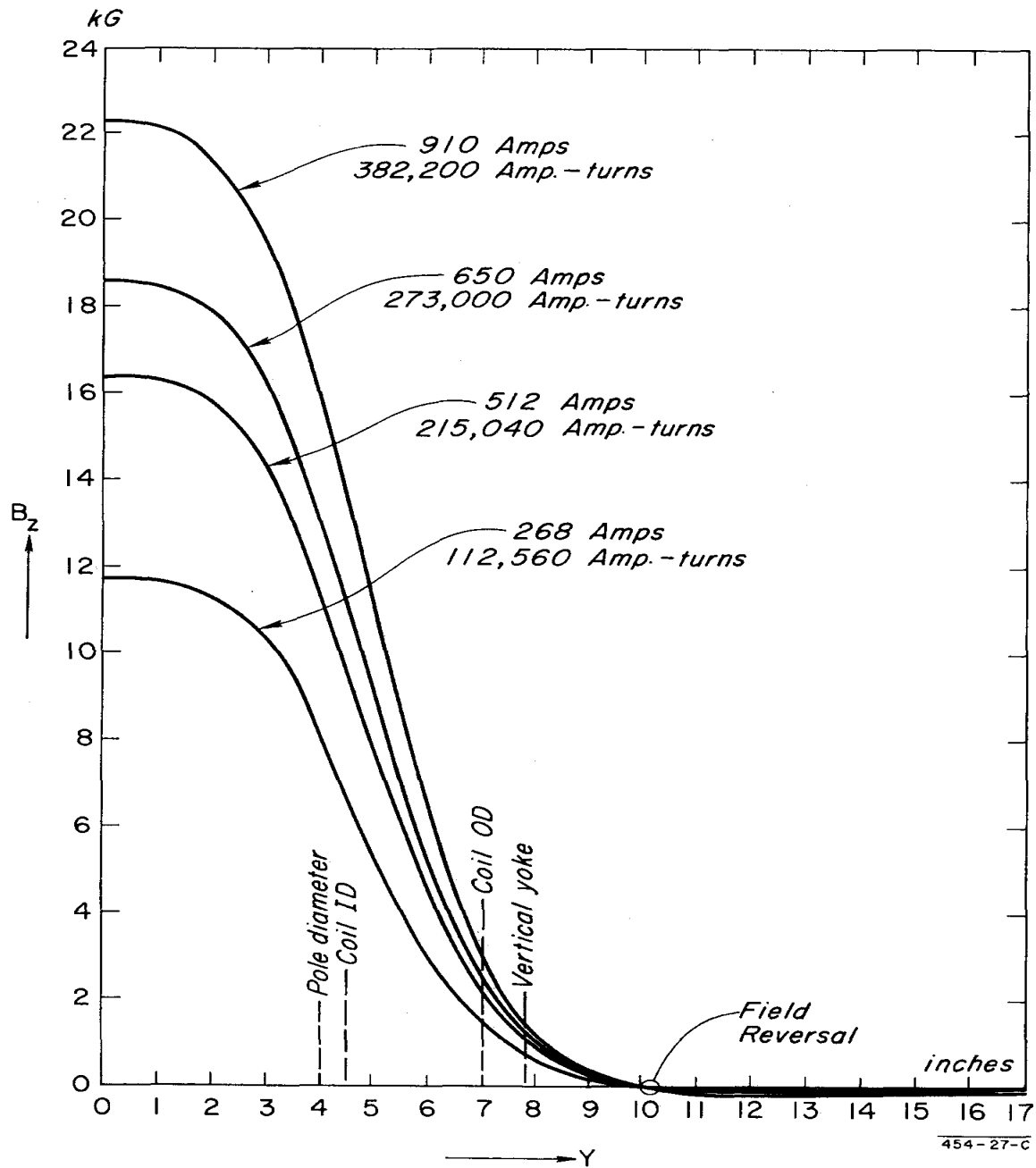


Fig. 17-- B_z along the Y axis for different excitation levels (magnet according to Fig. 15).

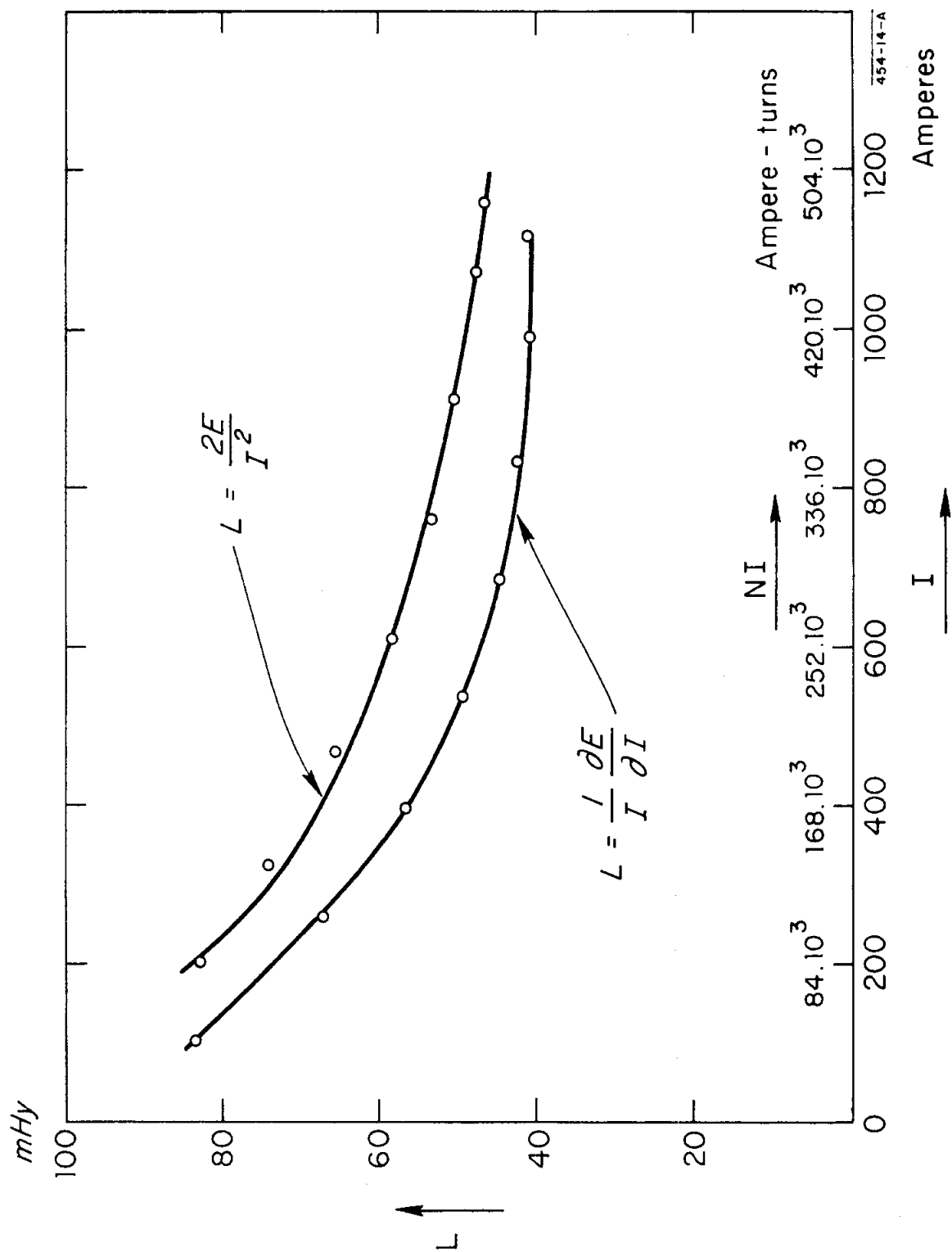


Fig. 18--Inductance versus excitation current (magnet according to Fig. 15).

C. Model with One Pole and Modified Upper Yoke

The top pole was removed. The upper horizontal yoke was provided with an 8.0-inch hole and the coils were arranged such that 9 double pancakes were provided for the upper coil and 5 double pancakes in the lower coil, as shown in Fig. 19.

The magnetization curve for this particular case is illustrated in Fig. 10, Curve V. It shows quite a substantial change from the symmetrical case.

The B_z field component versus the X coordinate of the median plane (2.25 inches above the pole surface) is given in Fig. 20 and versus the Y coordinate in Fig. 21 for various ampere-turn values.

In the X-Z plane the maximum field drop over half the pole diameter is 4.1% and over the entire pole is 24% at 4.36×10^5 ampere-turns excitation.

In the Y-Z plane the field drop over half the pole diameter is 3.6% and over the entire pole, 17.7%.

The magnet inductance is illustrated in Fig. 22.

D. Model with One Pole and Modified Upper Yoke Representing Final 2-Meter Spark Chamber Magnet

The number of double pancakes was reduced from 14 to 10. The total number of turns was 300; with a maximum current of 1.2×10^3 amps we obtained 1/10 of the ampere-turns of the 2-meter spark chamber magnet. The length of the vertical yokes was reduced accordingly in order to maintain the gap height of 4 inches (Fig. 23).

The curves $B_z = f(z)$ with $X = Y = 0$ are shown in Fig. 24 at various current levels. The tests indicate that the magnetic midplane is 2.2 inches above the pole surface. Measuring the radial field component along the x and y coordinates in the midplane is somewhat difficult, due primarily to our rather primitive field measuring installations.

The measurement errors due to the pickup coil positioning are estimated to be about 10%.

As illustrated in Fig. 25, the maximum B_r field along the x axis is ≈ 655 gauss, or 4.3% of the peak axial field $B_z(0,0,0)$. The peak occurs in the region between the top and bottom coils. The maximum value of B_r along the Y axis is about -400 gauss or about 2.6% of the axial field.

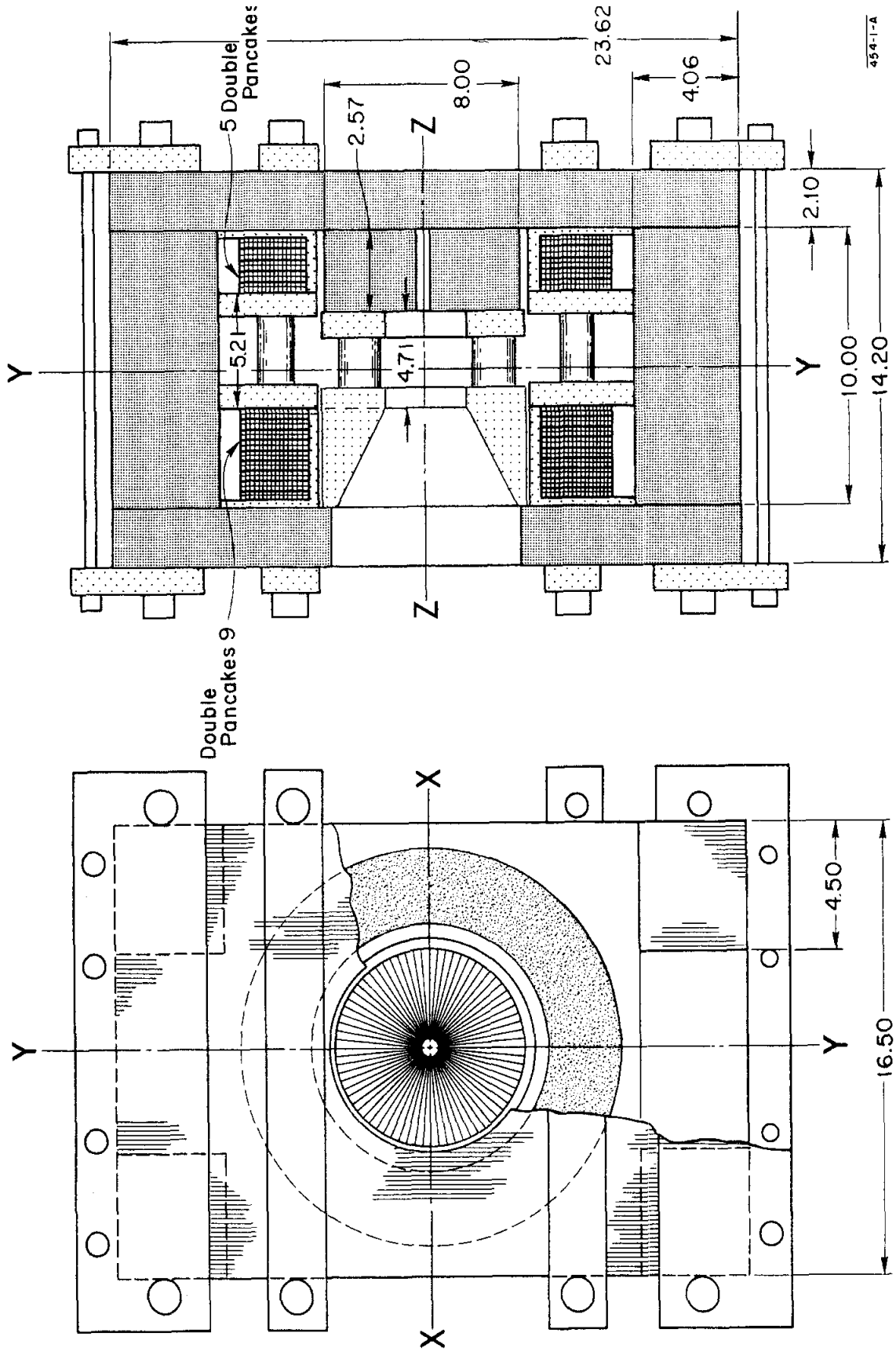


Fig. 19--Asymmetric model magnet. Upper pole removed. The upper yoke is provided with an opening of 8". Coils adjusted. Number of double pancakes 14.

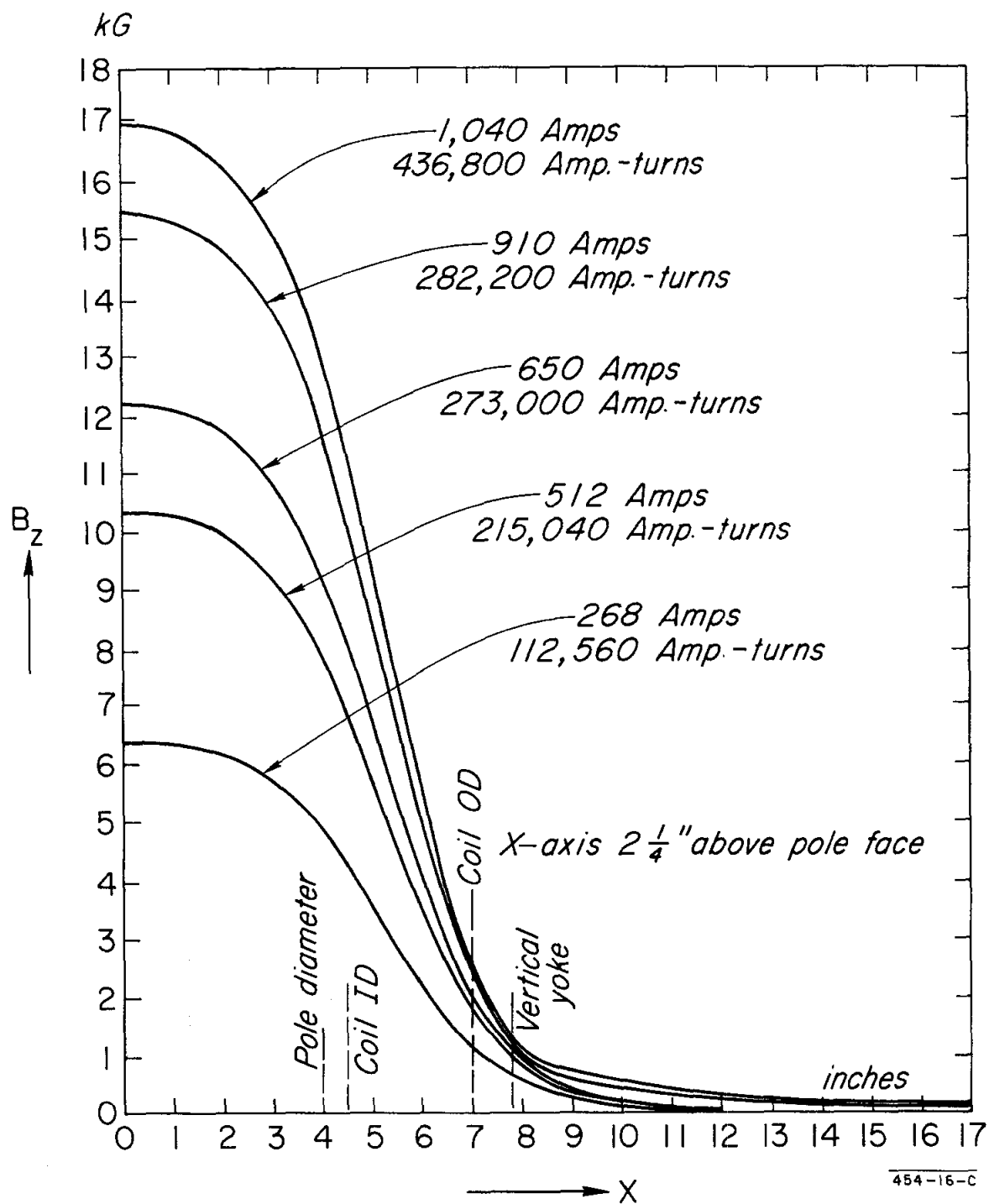


Fig. 20-- B_z distribution along X axis (magnet model Fig. 19).

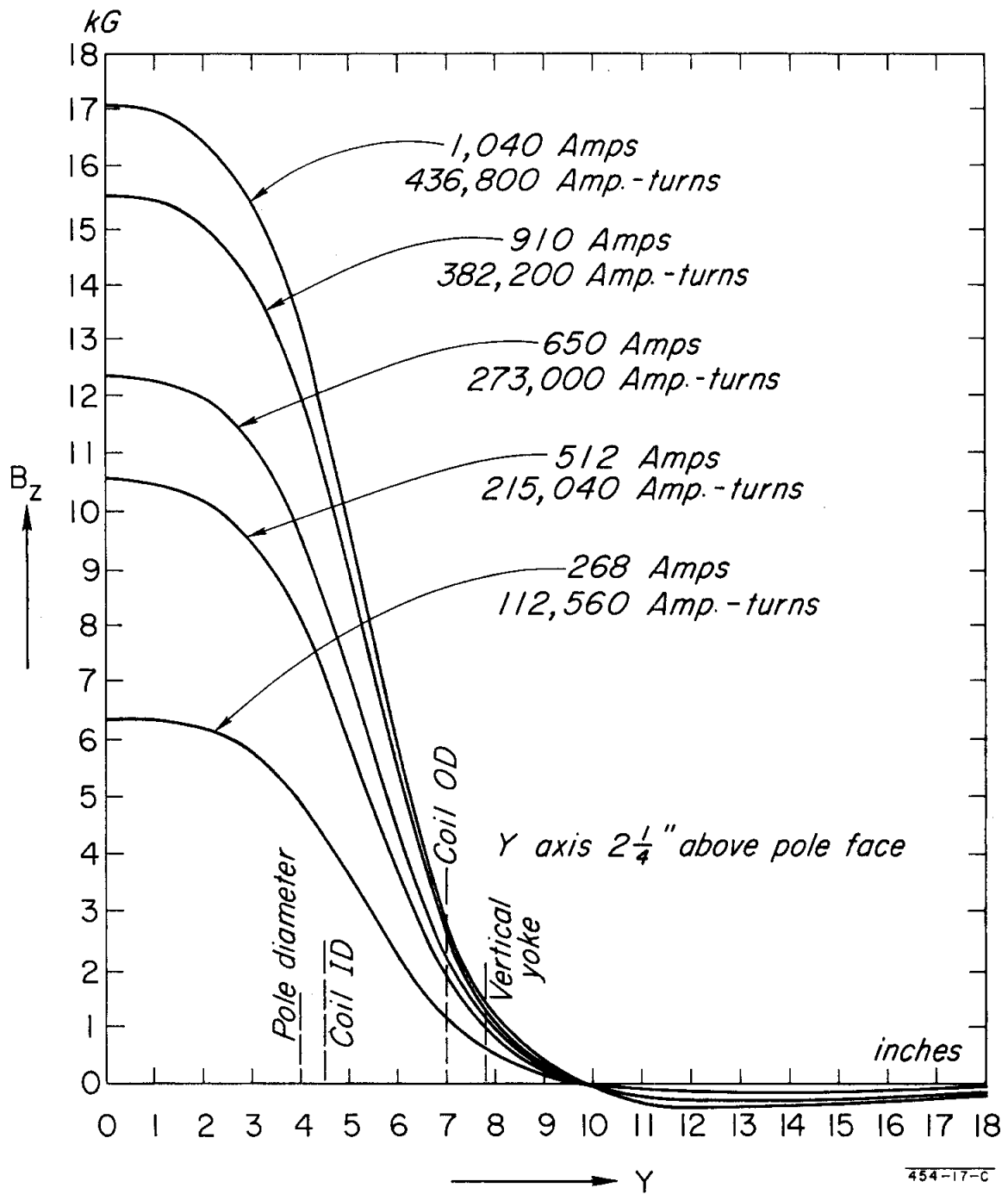


Fig. 21-- B_z distribution along Y axis (magnet model Fig. 19).

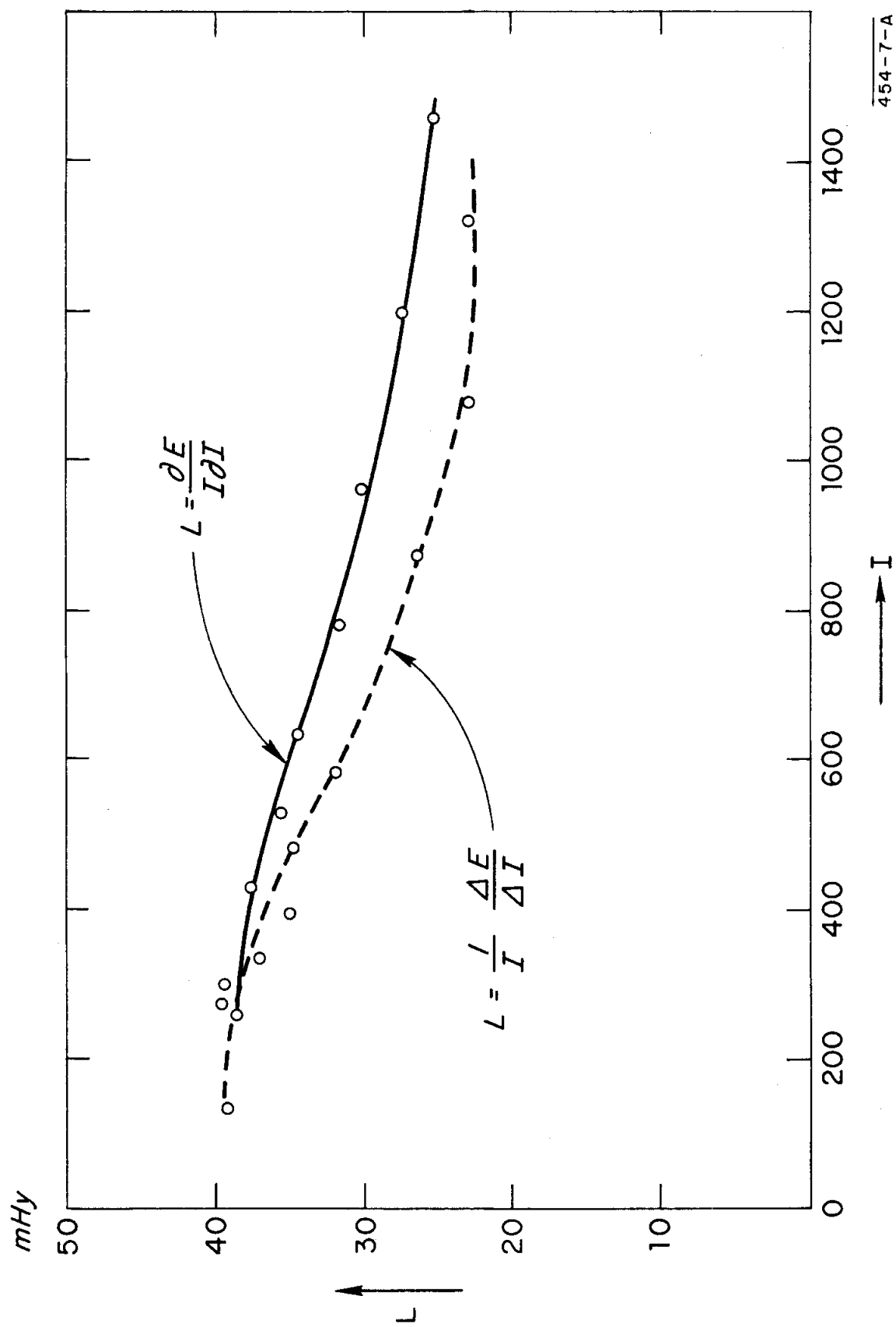


Fig. 22--Magnet inductance versus current (magnet model Fig. 19).

454-7-A

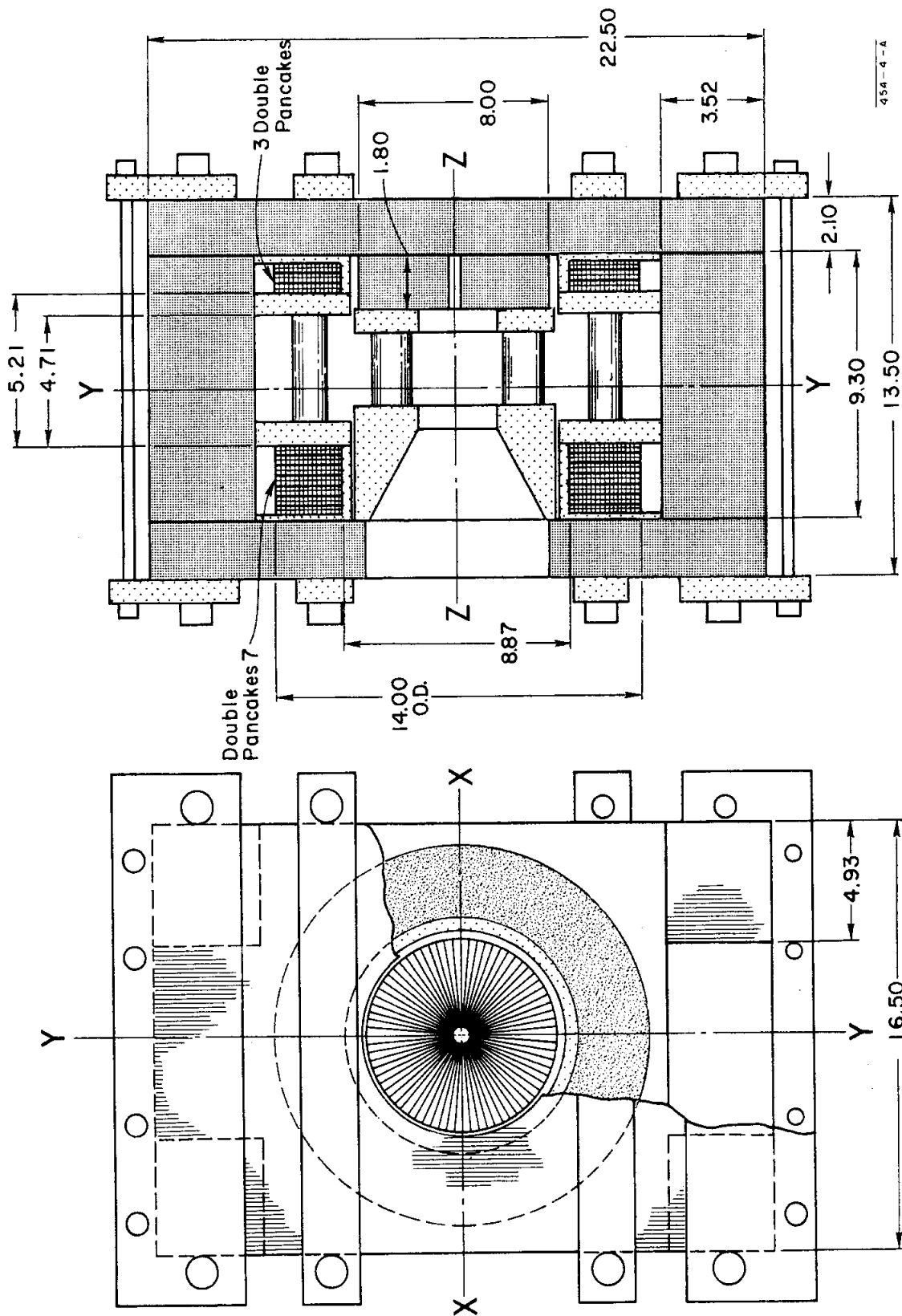


Fig. 23--Asymmetric model magnet (true 1/10 scale spark chamber magnet model shown in Fig. 1). Upper pole removed. Upper yoke provided with an opening of 8" diameter. Number of double pancakes is reduced from 14 to 10. Length of vertical yokes reduced to keep the gap height constant to 4".

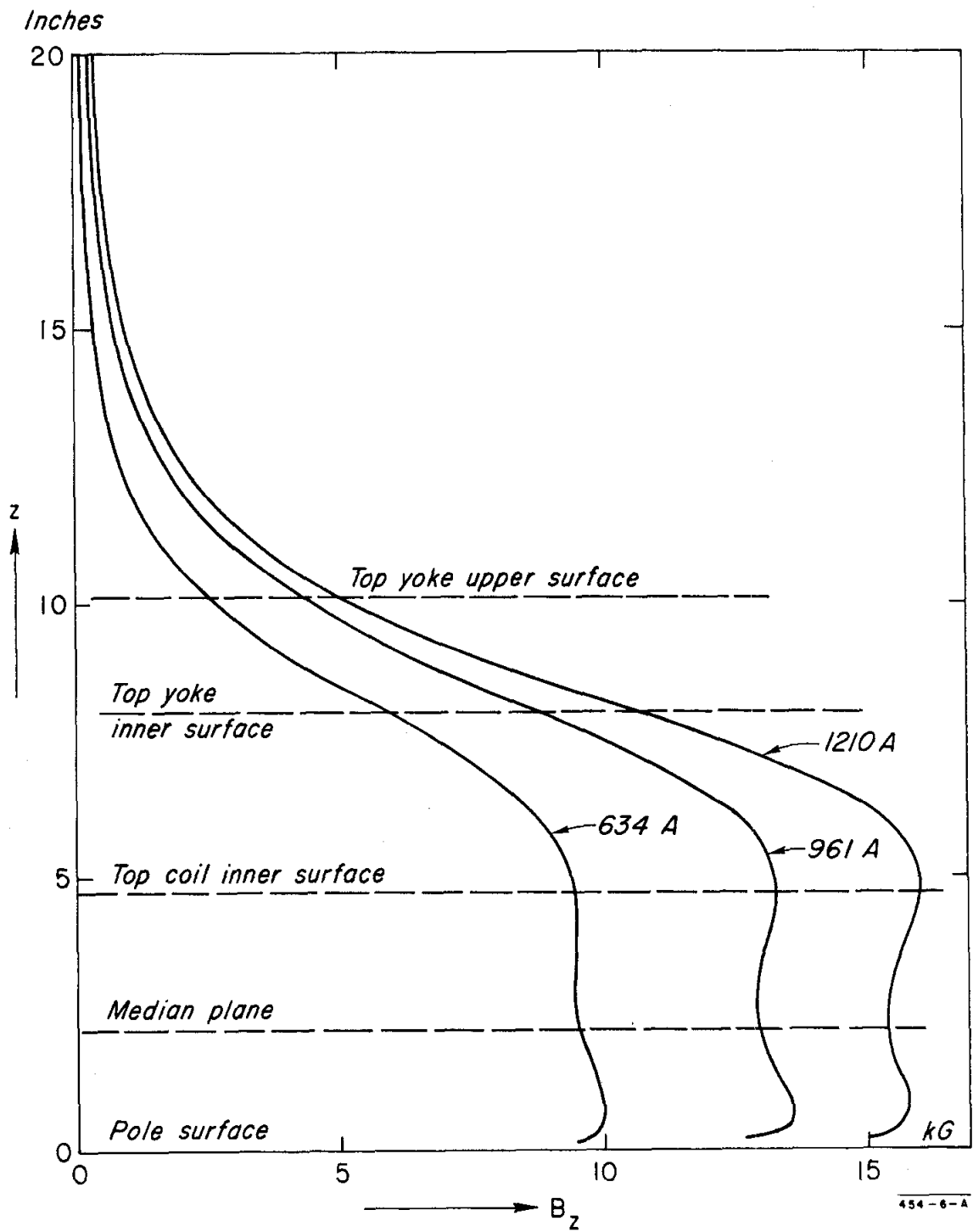
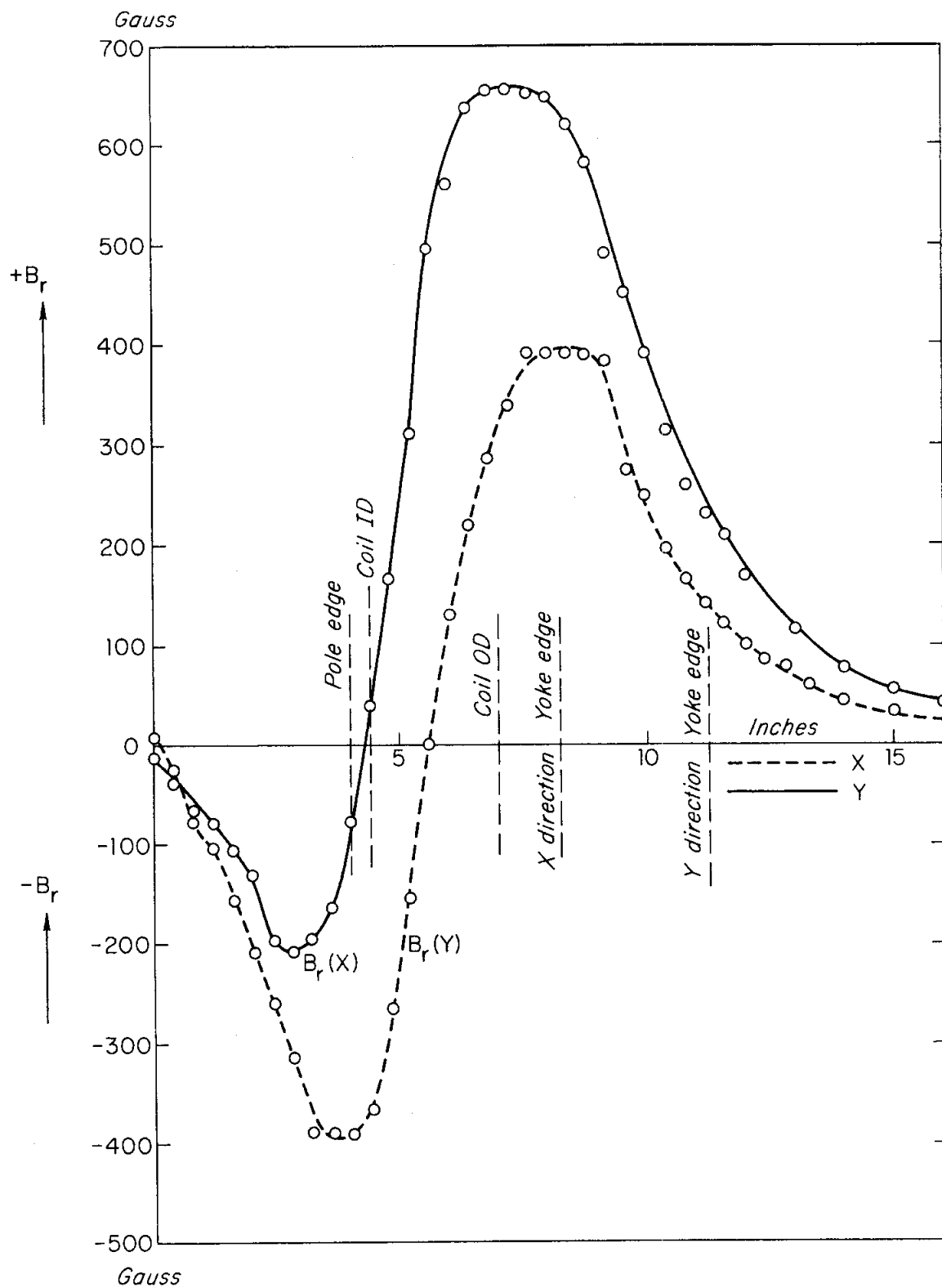


Fig. 24-- B_z versus Z axis for various magnet currents.



454-28-B

Fig. 25-- B_r versus X,Y measured in the median plane (magnet according to Fig. 2).

Curves of B_z close to the median plane, about 2.5 inches above the surface of the lower pole along the X and Y axis, are shown in Figs. 26 and 27. At maximum excitation, $\Delta B_z(x, 0) / B_z(0, 0) = 2.6\%$ at half the pole diameter and 18% at the pole edge.

The field deviation $\Delta B_z(0, y) / B_z(0, 0) = 2.6\%$ at half the pole diameter and 21% at the pole edge. Measurement of $B_z = f(x)$ close to the pole face is given in Fig. 28 and close to the upper coil in Fig. 29.

The field component above the upper yoke is shown in Fig. 30. The measurements were started at half the upper yoke height inside the opening at $x = 0$, $y = 3.625$ inches and $y = 0$, $x = 3.675$ inches. The magnet inductance versus excitation current is shown in Fig. 31.

The measurement gives a value of 21×10^{-3} Hy.

The sharp field drop at the pole center (Fig. 23) is due to an axial hole with a diameter of 0.375 inches.

IV. COMPARISON BETWEEN MEASUREMENT AND CALCULATIONS

As pointed out previously, it is difficult to simulate a rectangular-shaped magnet with complicated three-dimensional field distributions in a magnet with axial symmetry. The largest calculation errors occur due to the assumed location of the vertical yokes. If the field contribution due to the vertical yokes is neglected, the field at the center is approximately 13.9 kG, or 15.7% lower than the measured value. The total field contribution of iron would be 4.2 kG, which is on the low side.

Assuming that an iron shell of the same cross section as the four vertical yokes is placed around the coils, we get after 20 iterations a field of 14.6 kG at the center, which is about 5% lower than the measured value.

The fringing field is distorted; however, the axial and radial field distributions in the gap over the pole face comply with the measurements. A comparison between measured and calculated values is given below.

1. Position of the median plane

<u>Measurement</u>	55.8 cm above pole surface
<u>Calculation</u>	$\approx 52 - 55$ cm above pole surface

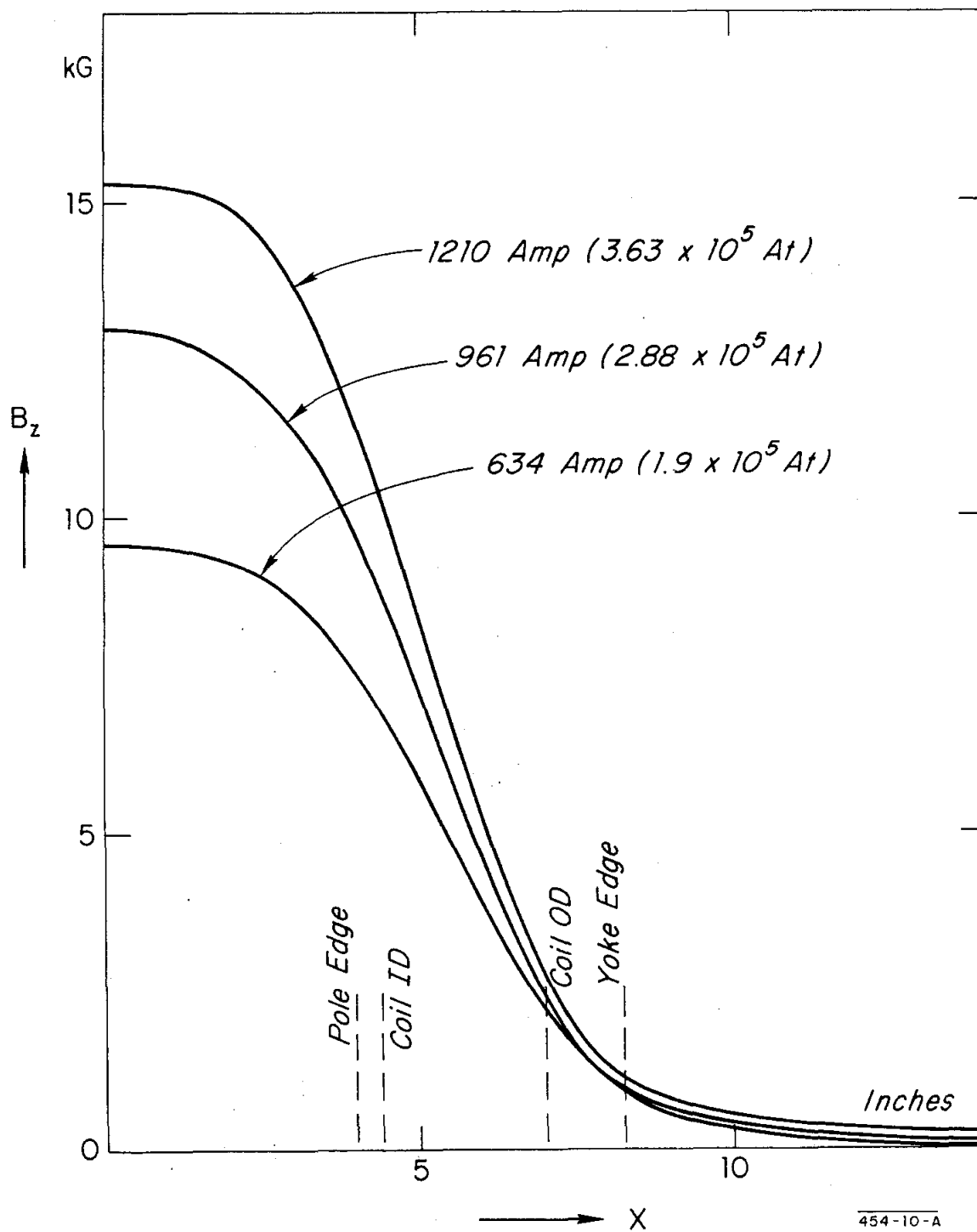


Fig. 26-- B_z along X axis (model magnet Fig. 23).

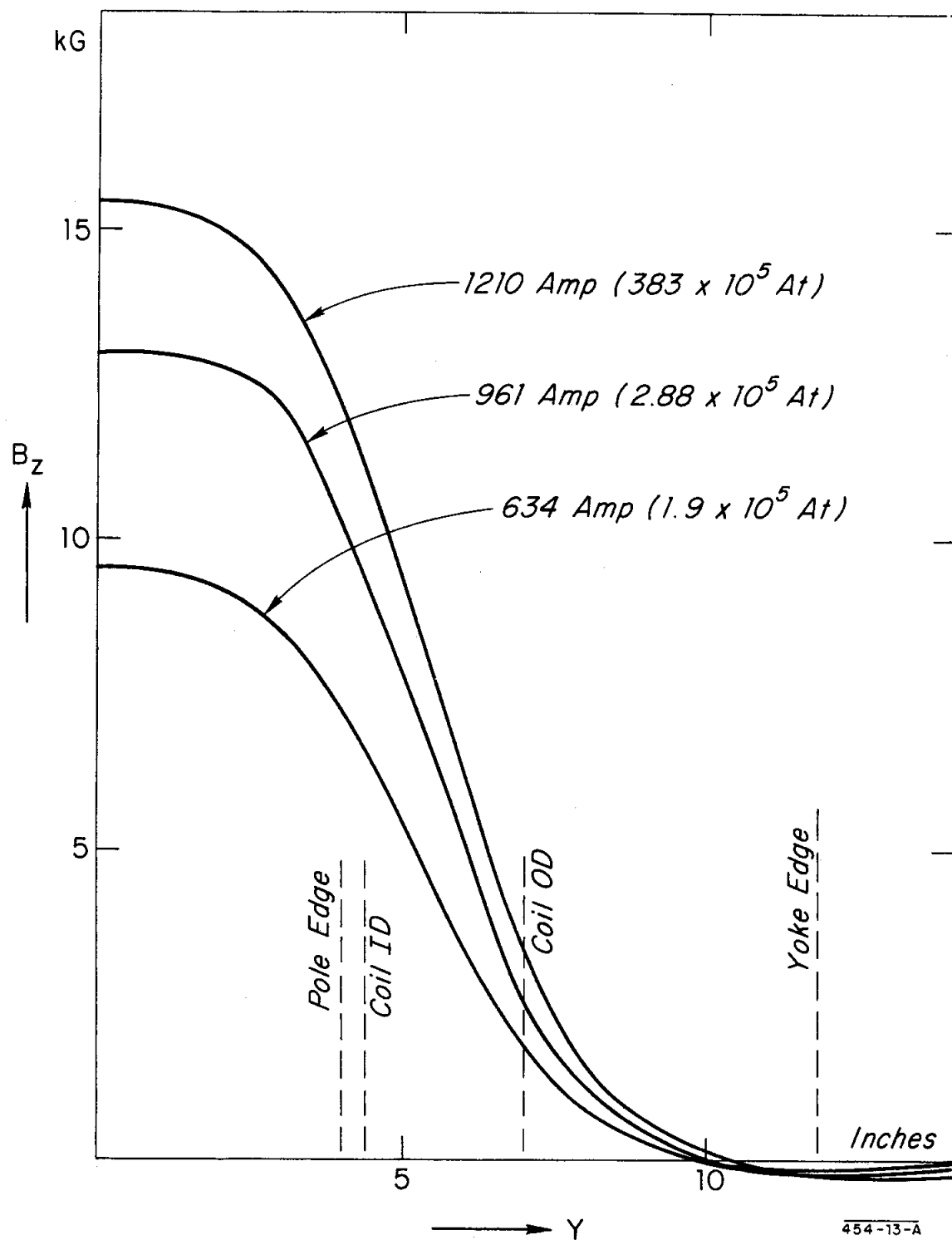


Fig. 27-- B_z along Y axis (model magnet Fig. 23).

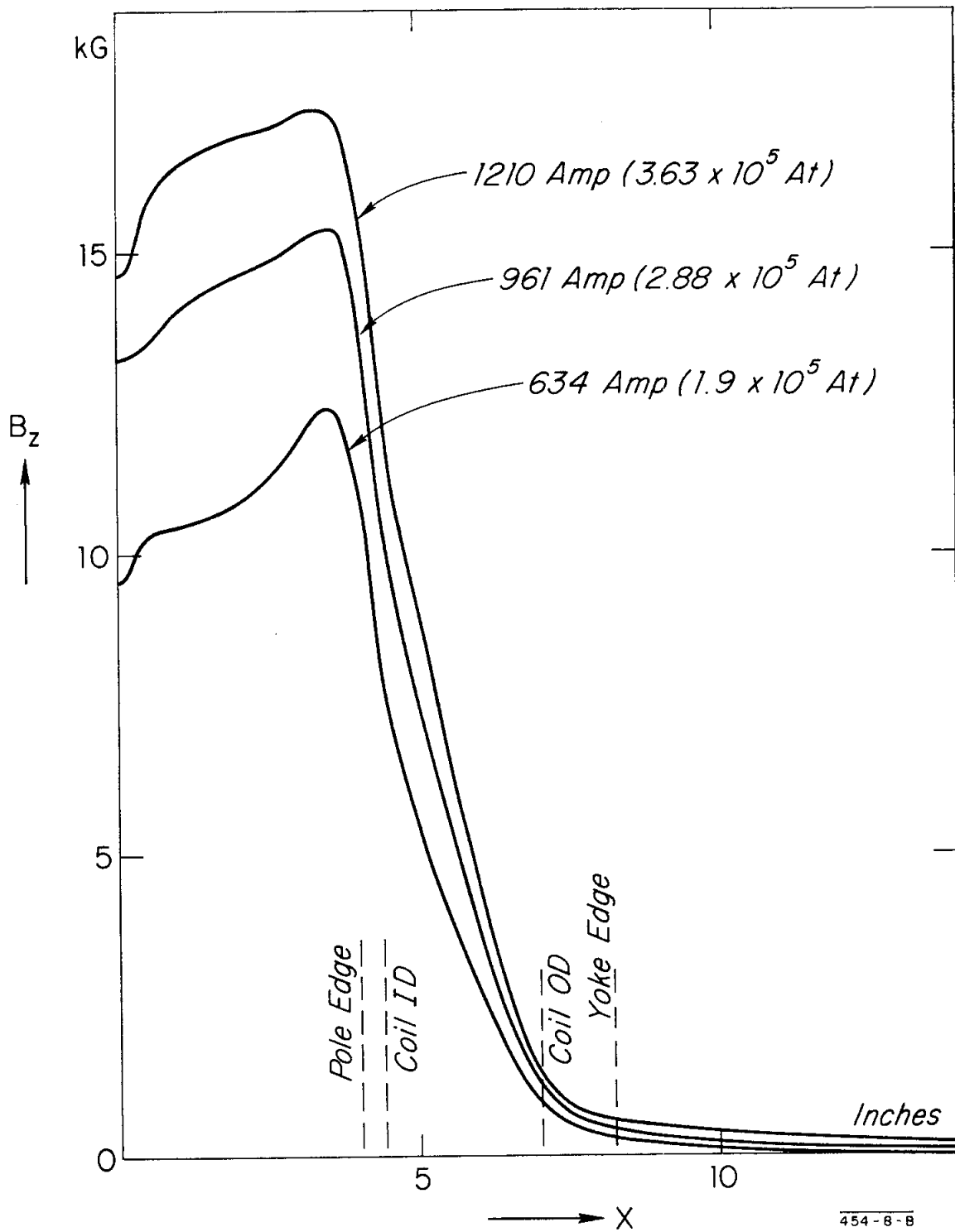


Fig. 28-- B_z versus X axis measured at $Z = 0.635$ cm above the pole surface.

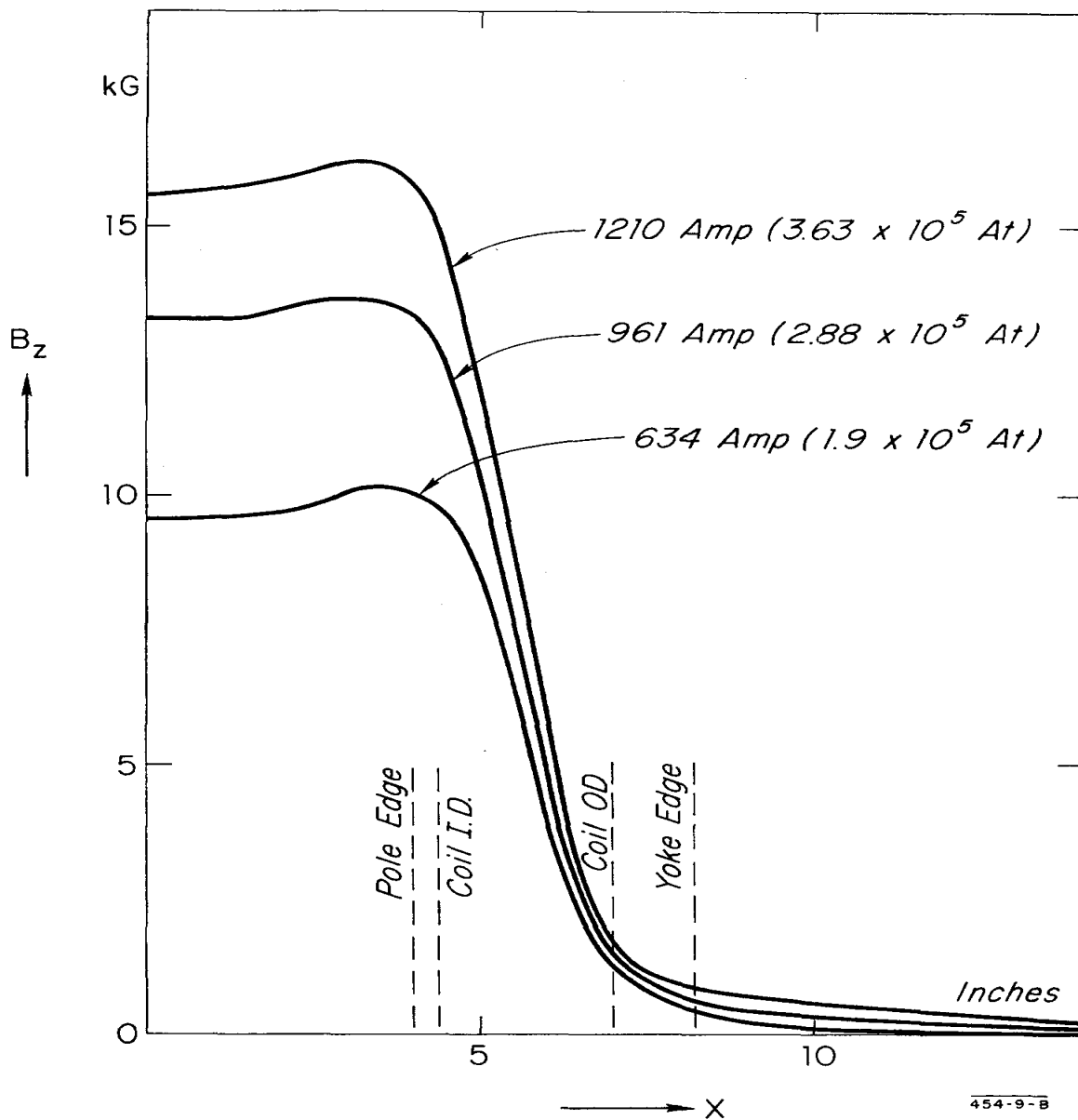


Fig. 29-- B_z versus X measured at $Z = 10.8$ cm above the pole surface.

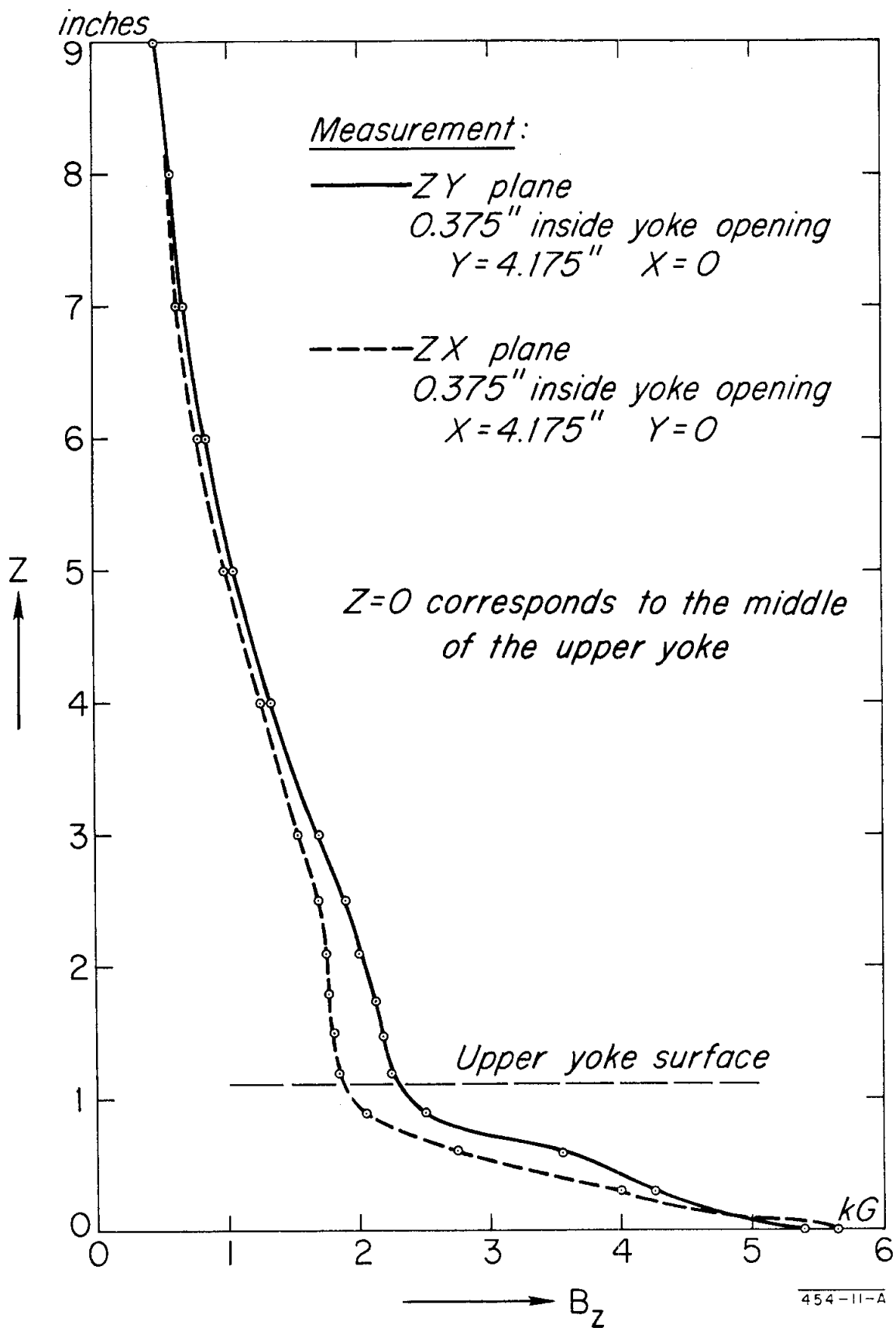


Fig. 30-- B_z versus Z axis above the upper yoke .

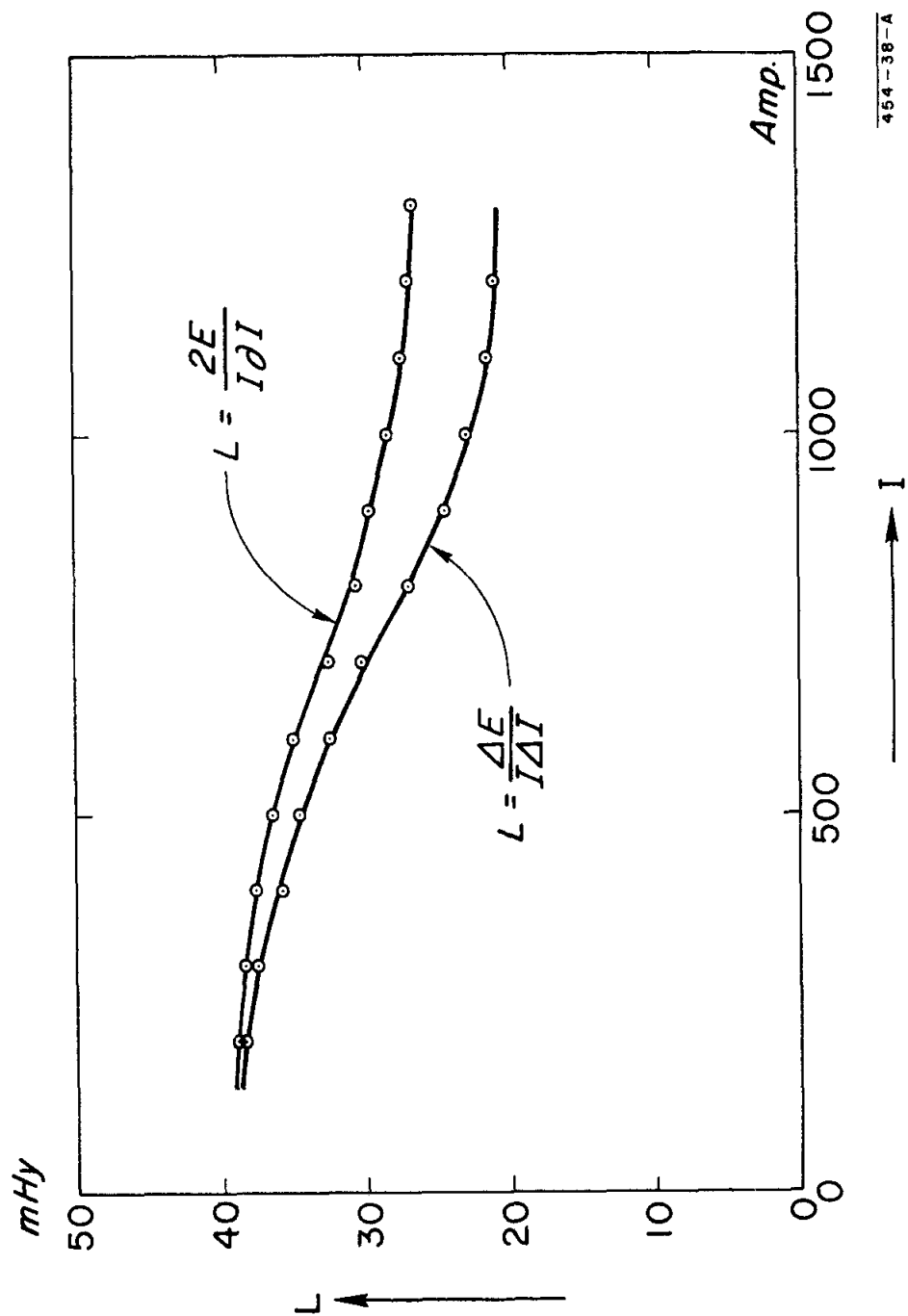


Fig. 31--Magnet inductance versus excitation current (model magnet Fig. 23).

2. Radial field components in the mid-plane

<u>Measurement</u>	$B_r = f(x)$	Max - 220 G inside gap Max + 660 G outside gap
	$B_r = f(y)$	Max - 390 G inside gap Max + 390 G outside gap
<u>Calculation</u>	$B_r = f(R)$	Max - 140 G inside gap
		Max + 1350 G outside gap

The calculation is performed at the assumed position of the median plane, 55 cm above the pole surface.

3. Axial field component in the median plane

<u>Measurements</u>	$B_z(x)$	Max 15.3 kG at $(x = y = 0)$
	$\frac{\Delta B}{B} = 0.0254$	at $x = 0.5R, y = 0$
	$\frac{\Delta B}{B} = 0.183$	at $x = R, y = 0$
	$B_z(y)$	Max 15.4 kG at $(x = y = 0)$
	$\frac{\Delta B}{B} = 0.0266$	at $y = 0.5 R, x = 0$
	$\frac{\Delta B}{B} = 0.207$	at $y = R, x = 0$

Note the 0.1 kG difference in the measurement of B_z in X and Y direction, which is the indication to measurement reproducibility.

Calculation

$B_z(r)$	Max 14.6 kG at $r = 0$
$\frac{\Delta B}{B} = 0.0068$	at $r = 0.5 R$
$\frac{\Delta B}{B} = 0.212$	at $r = R$

4. Axial field component off median plane

<u>Measurement</u>	in the plane 0.64 cm below the upper coil:	
	$B_{z, \max} = 15.6 \text{ kG}$	at $x = 0$
	$\frac{\Delta B}{B_o} = -0.04$	at $x = 0.66 R$

Calculation

$$B_{z, \max} = 14.8 \text{ kG} \quad \text{at } r = 0$$

$$\frac{\Delta B}{B} = -0.081 \quad \text{at } r = 0.86 R$$

Measurement in the plane 0.64 cm above lower pole:

$$B_{z, \max} = 14.6 \text{ kG} \quad \text{at } x = 0$$

$$\frac{\Delta B}{B} = -0.19 \quad \text{at } x = 0.86 R$$

Calculation

$$B_{z, \max} = 15.4 \text{ kG} \quad \text{at } r = 0$$

$$\frac{\Delta B}{B} = -0.25 \quad \text{at } r = 0.9 R$$

V. MODEL MEASUREMENTS

A. System Operation

A 360-pps triggering signal system is synchronized to the 60-cps power line and serves as a time reference to which all triggering circuits of the pulsing system are related. The trigger circuits are capable of operating at any pulse repetition frequency (PRF) from a single manual pulse up to 360 pulses per second, corresponding to the clock rate. For our magnet operation, however, the manual mode of operation was used exclusively.

The adjustable timing and delay circuit serves to sequence the automatic clock pulses according to the particular experiment. The operation cycle is explained with Fig. 32.

The 5-kV, 5-amp dc power supply charges the 60-kJ, 5-kV capacitor bank to any required voltage. The ignitron I_2 fires when triggered and the energy is discharged to the magnet.

The magnet control system is illustrated in the block diagram, Fig. 33.

When the voltage at the capacitor bank reaches zero volts, the start button is momentarily closed. The recharge gate supplies the pulse now to the grid of ignition I_1 . It also inhibits the firing gates for the ignitrons I_2 and I_3 . When the voltage at the capacitor bank reaches the desired voltage within $\pm 0.1\%$, as set by the voltage control unit, the recharge gate opens and energizes gates I_2 and I_3 . I_3 is normally delayed by the time set in the delay circuit. Current and voltage oscillograms for our particular magnet operation are shown in Fig. 35.

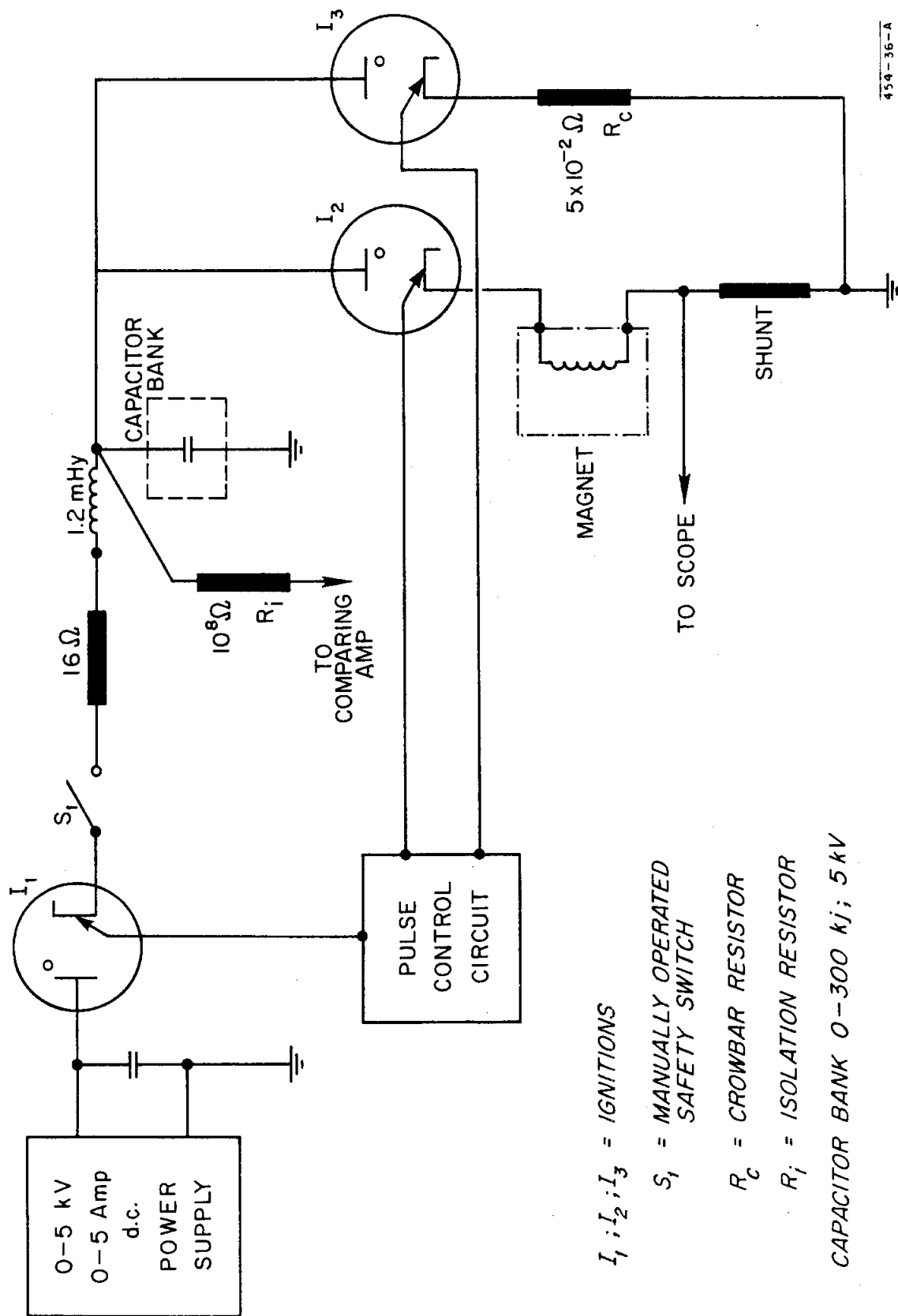
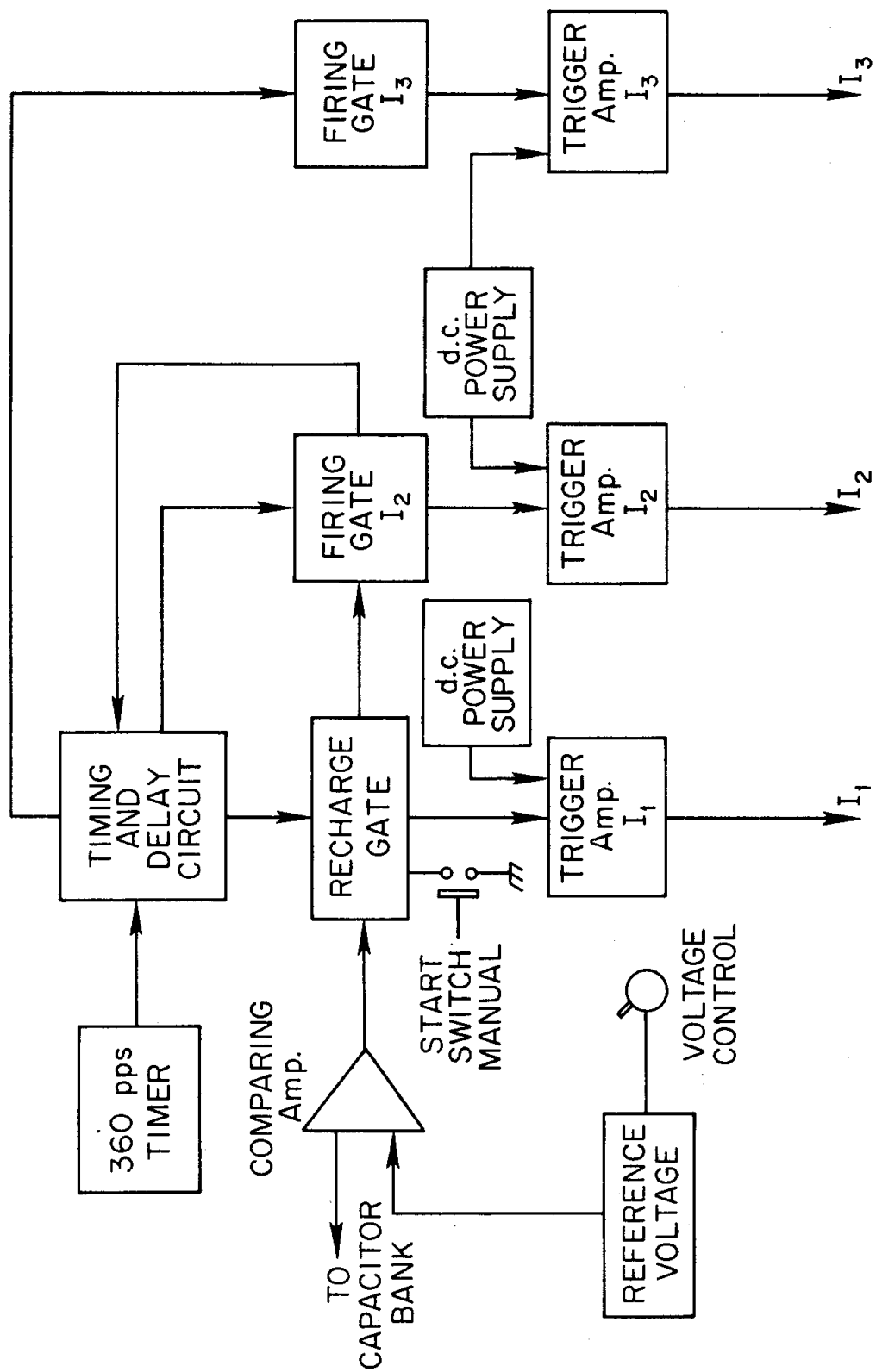


Fig. 32--Magnet pulser circuit.



454-35-A

Fig. 33--Magnet control system.

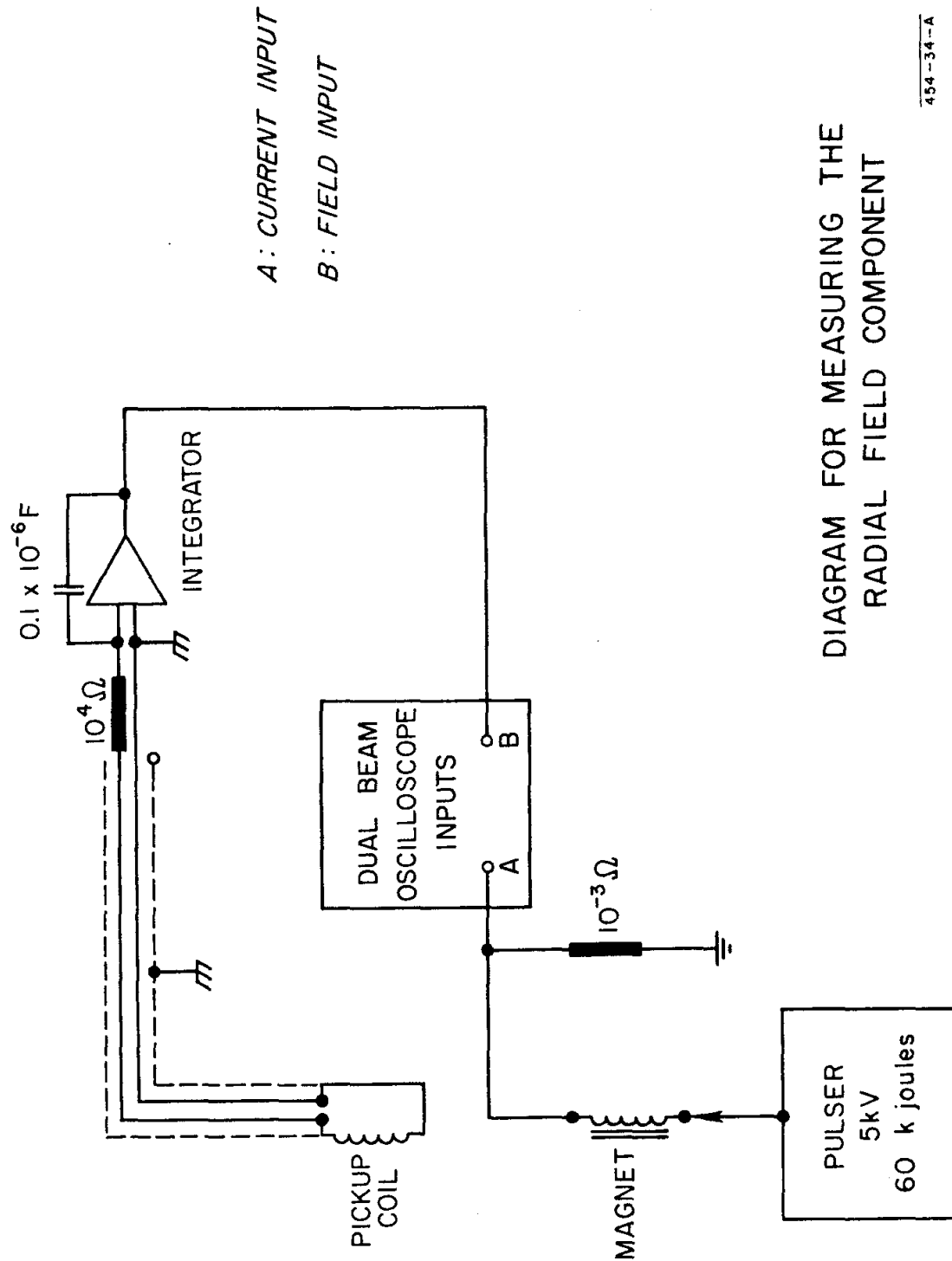
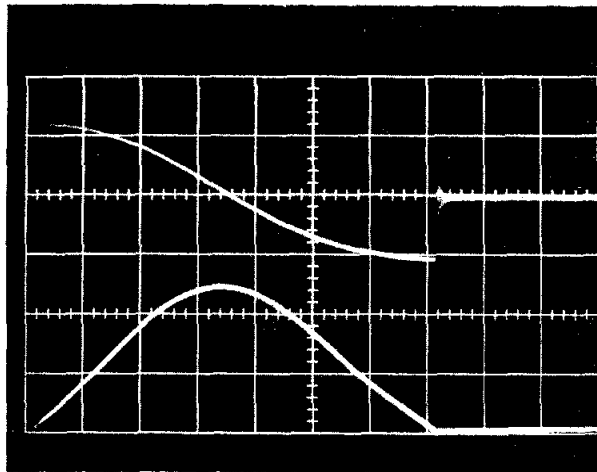


Fig. 34--Circuit to measure the radial field component.

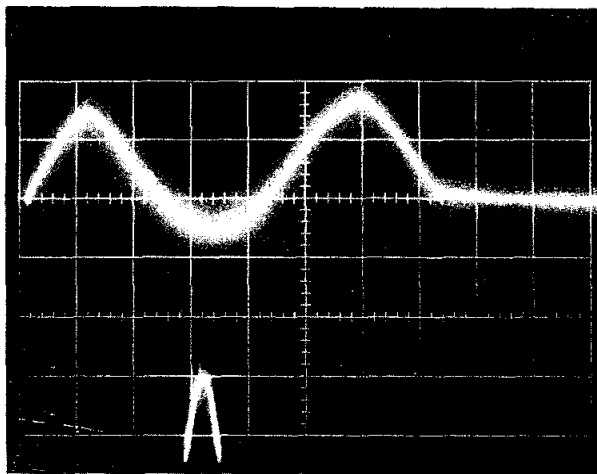
454-34-A



$I = 500 \text{ A/cm vertical}$
 $5 \text{ ms/cm horizontal}$

$V = 2500 \text{ V/cm vertical}$
 $5 \text{ ms/cm horizontal}$

Fig. 35--Axial field and current oscillograms .



$a - \text{Field}$

$b - \text{Peak current}$

454-5-A

Fig. 36--Radial field and peak current oscillograms.

Pick-up coils calibrated by means of a pretested known magnet were used for all the field measurements. The probable errors in the absolute values are estimated to be about 0.5%. The position error of the pick-up coil is about 1% for the axial field and about 10% in the measurements of the radial field component. The errors of the relative values are estimated to be about 0.4%.

B. Field Measurements

The test setup is shown schematically in Fig. 34. For radial field measurements, a small 0.95-cm i.d., 1.25-cm o.d., 0.8-cm-long pick-up coil was used in connection with a Miller integrator. All other field measurements were carried on using a integrating digital volt meter.

For the measurement of the radial component of the magnetic field, a dual beam oscilloscope was used to measure the output voltage of the Miller integrator, which is proportional to the instantaneous radial field component.

The sweep circuits of a dual beam oscilloscope were adjusted to show in one beam the peak of the pulsed current through the magnet coil and in the other beam the integrator output, corresponding to the magnet field. Both beams are time coincident and both traces are synchronized and adjusted such that peak field and current occur simultaneously. The corresponding peak field to the peak current can be photographed as shown in Fig. 36. The measurement errors are caused primarily by the coil positioning, which may be due to angular deviations exceeding 10%. The current and field errors are less than 10^{-3} .

ACKNOWLEDGEMENT

The authors are indebted to Prof. R. Mozley, SLAC, who supported this program and helped with many suggestions and discussions; and to Mr. R. Bell and Mr. L. Schwarcz for their help in providing necessary information and for their cooperation.

APPENDIX A

AXIAL AND RADIAL FIELDS OF COAXIAL SOLENOID PAIRS

The azimuthal component of the magnetic vector potential A_θ for a solenoid is written as (refer to Fig. 37)

$$A_\theta = \frac{\mu}{4\pi} S\lambda \int_{-b_1}^{+b_1} db \int_{a_1}^{a_2} a da \int_0^{2\pi} \frac{\cos \phi d\phi}{\left[(z-b)^2 + r^2 + a^2 - 2ar \cos \phi\right]^{\frac{1}{2}}} \quad (A-1)$$

With the notation

$$\xi = z - b$$

$$\xi_1 = z - b_1$$

$$\xi_2 = z + b_1$$

we obtain:

$$A_\theta = \frac{\mu S\lambda}{4\pi} \int_{a_1}^{a_2} a da \int_0^{2\pi} \cos \phi \ln \left[\xi + (\xi^2 + r^2 + a^2 - 2ar \cos \phi)^{\frac{1}{2}} \right] d\phi \bigg|_{\xi_1}^{\xi_2} \quad (A-2)$$

Because

$$B_r = - \frac{\partial A_\theta}{\partial z}$$

$$B_z = \frac{1}{r} A_\theta + \frac{\partial A_\theta}{\partial r}$$

we get:

$$B_z = \frac{\mu S\lambda}{4\pi} \int_{a_1}^{a_2} a da \int_0^{2\pi} \frac{\xi(a-r \cos \phi) d\phi}{(a^2 + r^2 - 2ar \cos \phi)(\xi^2 + r^2 + a^2 - 2ar \cos \phi)^{\frac{1}{2}}} \bigg|_{\xi_1}^{\xi_2} \quad (A-3)$$

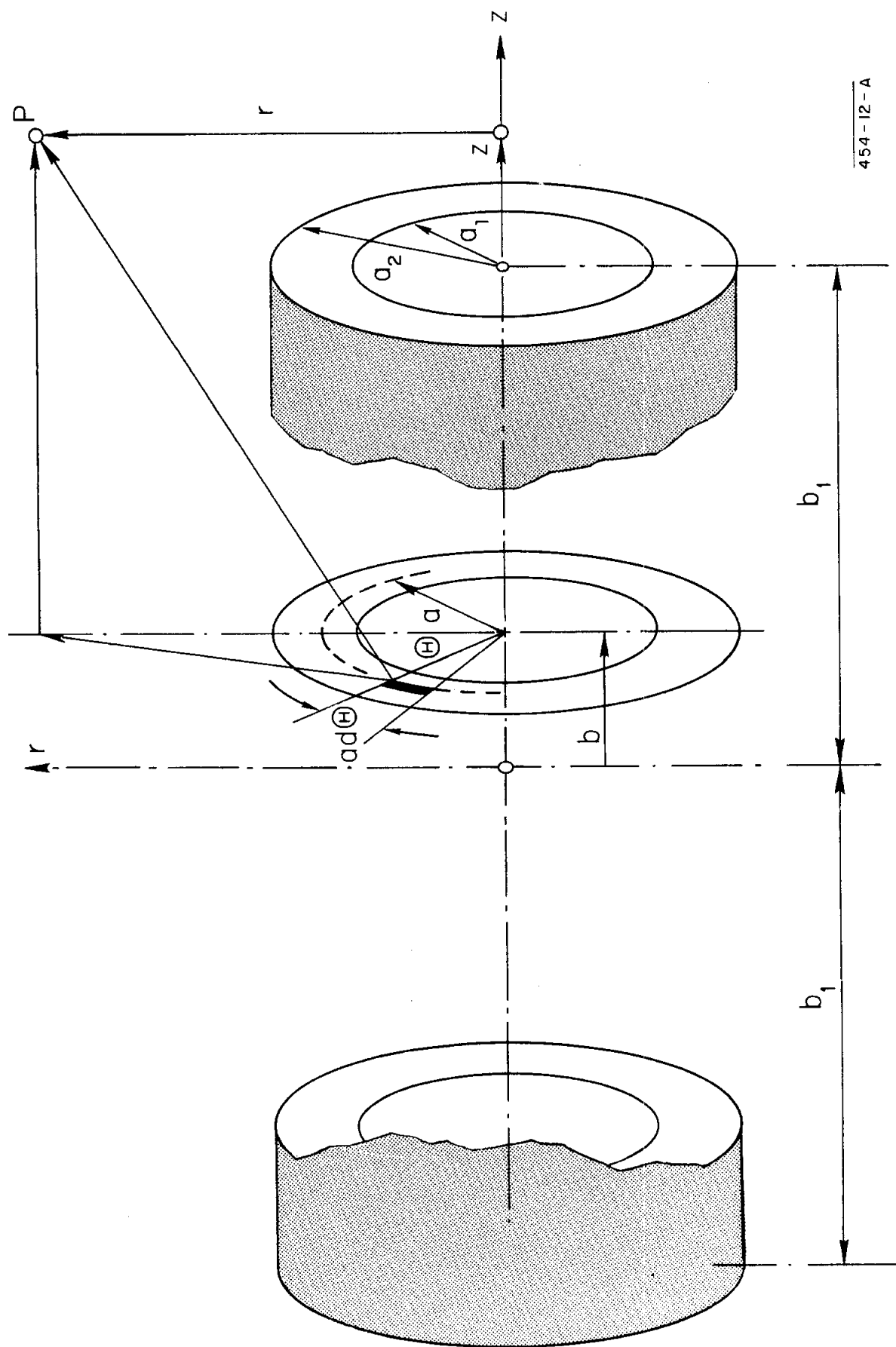


Fig. 37 --Coil representation for calculation purposes.

and

$$B_r = -\frac{\mu S \lambda}{4\pi} \int_{a_1}^{a_2} da \int_0^\pi \frac{\cos \phi d\phi}{(\xi^2 + r^2 + a^2 - 2ar \cos \phi)^{\frac{1}{2}}} \Big|_{\xi_1}^{\xi_2} \quad (A-4)$$

At a point along the symmetry axis $r \equiv 0$:

$$B_r = 0$$

and

$$B_z = \frac{\mu}{2} S \lambda \int_{a_1}^{a_2} \left[\frac{\xi_2 da}{(\xi_2^2 + a^2)^{\frac{1}{2}}} - \frac{\xi_1 da}{(\xi_1^2 + a^2)^{\frac{1}{2}}} \right] \quad (A-5)$$

$$= \frac{\mu}{2} S \lambda \cdot \left\{ (z + b_1) \cdot \ln \frac{a_2 + [a_2^2 + (z + b_1)^2]^{\frac{1}{2}}}{a_1 + [a_1^2 + (z + b_1)^2]^{\frac{1}{2}}} \right. \\ \left. + (b_1 - z) \cdot \ln \frac{a_2 + [a_2^2 + (b_1 - z)^2]^{\frac{1}{2}}}{a_1 + [a_1^2 + (b_1 - z)^2]^{\frac{1}{2}}} \right\} \quad (A-6)$$

In terms of dimensionless parameters this becomes

$$B_z = \frac{\mu}{2} S \lambda \cdot a_1 \left\{ (\gamma + \beta) \ln \frac{\alpha + [\alpha^2 + (\gamma + \beta)^2]^{\frac{1}{2}}}{1 + [1 + (\gamma + \beta)^2]^{\frac{1}{2}}} \right. \\ \left. + (\beta - \gamma) \cdot \ln \frac{\alpha + [\alpha^2 + (\beta - \gamma)^2]^{\frac{1}{2}}}{1 + [1 + (\beta - \gamma)^2]^{\frac{1}{2}}} \right\} \quad (A-7)$$

For a pair of solenoids Eq. (A-7) may be extended

$$B_z = \frac{\mu}{2} S \lambda a_1 \left\{ \begin{aligned} & (\gamma_1 + \beta_1) \ln \frac{\alpha + [\alpha^2 + (\gamma_1 + \beta_1)^2]^{\frac{1}{2}}}{1 + [1 + (\gamma_1 + \beta_1)^2]^{\frac{1}{2}}} \\ & - (\gamma_1 - \beta_1) \ln \frac{\alpha + [\alpha^2 + (\gamma_1 - \beta_1)^2]^{\frac{1}{2}}}{1 + [1 + (\gamma_1 - \beta_1)^2]^{\frac{1}{2}}} \\ & + (\gamma_2 + \beta_1) \ln \frac{\alpha + [\alpha^2 + (\gamma_2 + \beta_2)^2]^{\frac{1}{2}}}{1 + [1 + (\gamma_1 + \beta_1)^2]^{\frac{1}{2}}} \\ & - (\gamma_2 - \beta_2) \ln \frac{\alpha + [\alpha^2 + (\gamma_1 - \beta_1)^2]^{\frac{1}{2}}}{1 + [1 + (\gamma_1 - \beta_1)^2]^{\frac{1}{2}}} \end{aligned} \right\} \quad (A-8)$$

$$B_z = \frac{\mu}{2} S \lambda a_1 \cdot F(\alpha; \beta_1; \beta_2; \gamma_1; \gamma_2)$$

or, in terms of ampere-turns,

$$B_z = \frac{\mu}{4} \cdot \frac{NI}{a_1(\alpha-1)(\beta_1 + \beta_2)} \cdot F(\alpha; \beta_1; \beta_2; \gamma_1; \gamma_2)$$

The power requirement in the coil maybe expressed as:

$$P = 2\pi a_1^3 S^2 \rho (\alpha^2 - 1)(\beta_1 + \beta_2) \cdot \lambda \quad (A-9)$$

Eliminating the current density S from (A-8) and (A-9) we get:

$$B_z = \frac{\sqrt{2\pi}}{10} \cdot \frac{F}{\sqrt{(\alpha^2 - 1)(\beta_1 + \beta_2)}} \cdot \sqrt{\frac{P\lambda}{a_1 \rho}} \quad (A-10)$$

with B_z expressed in gauss, a_1 in cm, ρ in ohm·cm and P in watts.

APPENDIX B THE GEOMETRICAL MODEL

We shall designate coordinates, magnetic and electric intensities, conductivity, flux density, etc., of the original magnet with one prime, such as ℓ' , t' , H' , E' , B' , etc., and the corresponding quantities of the model with double primes, such as ℓ'' , t'' , H'' , B'' , etc. The reduction ratio can be expressed as:

$$\ell = \frac{\ell''}{\ell'} ; \quad t = \frac{t''}{t'} ; \quad B = \frac{B''}{B'} \quad \text{etc.}$$

Consider Maxwell's equations for the original:

$$\nabla \times H' = \kappa' E' + \epsilon' \frac{\partial E'}{\partial t'} \quad (B-1)$$

$$\nabla \times E' = -\mu' \frac{\partial H'}{\partial t'} \quad (B-2)$$

$$B' = \mu' H' \quad \nabla B' = 0 \quad (B-3)$$

$$D' = \epsilon' E' \quad \nabla D' = 4\pi \rho' \quad (B-4)$$

From Eq. (B-1) we obtain

$$\nabla \times \nabla \times H' = \kappa' \nabla \times E' + E' + \epsilon' \nabla \times \frac{\partial E'}{\partial t'} \quad (B-5)$$

Using Eq. (B-2) and modifying Eq. (B-5), we get

$$\nabla^2 H' = \mu' \kappa' \frac{\partial H'}{\partial t'} - \epsilon' \mu' \frac{\partial^2 H'}{\partial t'^2} \quad (B-6)$$

With $H' = H'_0 \cdot e^{j\omega' t'}$ we get from Eq. (B-6)

$$\nabla^2 H' = (j\kappa' \mu' \omega'_0 - \epsilon' \mu' \omega'^2_0) H'_0 \quad (B-7)$$

If the model is scaled down by ℓ , permeability μ , conductivity κ , and frequency ω , etc., we get

$$\frac{H}{\ell^2} \nabla^2 H' = \kappa \mu \omega (H j \kappa' \mu' \omega'_0) - \epsilon \mu \omega^2 H (\epsilon' \mu' \omega'^2_0) H'_0 \quad (B-8)$$

Equation (B-8) is possible only if

$$\frac{H}{\ell^2} = \kappa \mu \omega H = \epsilon \mu \omega^2 H \quad (B-9)$$

or

$$\kappa \mu \omega \ell^2 = 1$$

$$\epsilon \mu \omega^2 \ell^2 = 1$$

For:

$$\epsilon = \mu = 1$$

$$\omega = \frac{1}{\ell} \quad \text{or} \quad t = \ell$$

$$\kappa = \frac{1}{\ell}$$

In the geometrical model the time scale and the resistivity factor must be proportional to the length scale, which makes the geometrical model impractical.

APPENDIX C

THE ELECTROMAGNETIC MODEL³

The model windings and core are assumed to be geometrically similar to the original, with the length scale factor ℓ .

The turn ratio of the model to the original is constant and equal to N . The space factor should be nearly the same. In the electro-magnetic model all quantities may be different from the corresponding quantities of the original, except for the magnetic state of the core at corresponding times.

$$B''(t'') = B'(t') \quad (C-1)$$

$$H''(t'') = H'(t') \quad (C-2)$$

For the induced electromotive force we can write:

$$V' = - N' A' \frac{dB'}{dt'} \quad (C-3)$$

$$V' = - N'' A'' \frac{dB''}{dt''} \quad (C-4)$$

$$V = \frac{1}{t} NA = \frac{1}{t} N\ell^2 \quad (C-5)$$

and for the magnetomotive force:

$$N' I' = \frac{1}{\mu} \cdot H' \delta' \quad (C-6)$$

$$N'' I'' = \frac{1}{\mu} H'' \delta'' \quad (C-7)$$

which gives, with Eq. (C-2),

$$I = \frac{\delta}{N} = \frac{\ell}{N} \quad (C-8)$$

The resistance ratio, from Eq. (C-5) and (C-8)

$$Z = R = \frac{V}{I} = \frac{\ell N^2}{t} \quad (C-9)$$

The inductance is

$$L = \frac{Z}{\omega} = tZ = \ell N^2 \quad (C-10)$$

and the capacitance is

$$C = \frac{t}{Z} = \frac{t^2}{\ell N^2} \quad (C-11)$$

In the electromagnetic model we may choose three scale factors arbitrarily. All other factors are established by dimensional analysis.

REFERENCES

1. G. Bonzano and G. Petrucci, "2-Meter Hydrogen Bubble Chamber Magnet Measures on the Magnet Model," CERN Internal Report 135, CERN, Geneva (1960).
2. E. A. Burfine, L. R. Anderson and H. Brechna, "A Computer Code for Variable Permeability Magnetostatic Field Problems," SLAC Report No. 56, Stanford Linear Accelerator Center, Stanford, California (1966).
3. P. A. Abetti, "Transformer Models for the Determination of Transient Voltages," AIEE Trans. Part III, No. 6, pp. 468-480 (1953).
4. H. Brechna, "A Pulsed Bending Magnet for the Beam Switchyard Area of the Stanford Two-Mile Linear Accelerator," SLAC Report No. 28, Stanford Linear Accelerator Center, Stanford, California (1964), pp. 36-41.
5. R. Mozley, "Two-Meter Spark Chamber Magnet," SLAC Internal Report, Stanford Linear Accelerator Center, Stanford, California (1965).
6. F. Bitter, Rev. Sci. Instr. 7, 482-488 (1936).
7. L. R. Anderson, D. G. Borglum, and E. A. Burfine, "The Calculation of Magnetic Fields from Solenoids and Iron at Any Point in Space," SLAC Internal Report, Stanford Linear Accelerator Center, Stanford, California (1965).
8. H. Brechna, "Electromagnets for High Energy Physics Applications," Proceedings of the International Symposium on Magnet Technology, Stanford Linear Accelerator Center, September 8-10, 1965; pp. 1-26.